










ARTICLE

# Sarm1 activation produces cADPR to increase intra-axonal $\text{Ca}^{++}$ and promote axon degeneration in PIPN

Yihang Li<sup>1,2</sup>, Maria F. Pazyra-Murphy<sup>1,2</sup>, Daina Avizonis<sup>3</sup> , Mariana de Sá Tavares Russo<sup>3</sup> , Sophia Tang<sup>2</sup>, Chiung-Ya Chen<sup>4</sup>, Yi-Ping Hsueh<sup>4</sup> , Johann S. Bergholz<sup>2,5,6</sup>, Tao Jiang<sup>2</sup>, Jean J. Zhao<sup>2,5,6</sup> , Jian Zhu<sup>7</sup> , Kwang Woo Ko<sup>8</sup> , Jeffrey Milbrandt<sup>7,9</sup> , Aaron DiAntonio<sup>8,9</sup> , and Rosalind A. Segal<sup>1,2</sup> 

**Cancer patients frequently develop chemotherapy-induced peripheral neuropathy (CIPN), a painful and long-lasting disorder with profound somatosensory deficits. There are no effective therapies to prevent or treat this disorder. Pathologically, CIPN is characterized by a “dying-back” axonopathy that begins at intra-epidermal nerve terminals of sensory neurons and progresses in a retrograde fashion. Calcium dysregulation constitutes a critical event in CIPN, but it is not known how chemotherapies such as paclitaxel alter intra-axonal calcium and cause degeneration. Here, we demonstrate that paclitaxel triggers Sarm1-dependent cADPR production in distal axons, promoting intra-axonal calcium flux from both intracellular and extracellular calcium stores. Genetic or pharmacologic antagonists of cADPR signaling prevent paclitaxel-induced axon degeneration and allodynia symptoms, without mitigating the anti-neoplastic efficacy of paclitaxel. Our data demonstrate that cADPR is a calcium-modulating factor that promotes paclitaxel-induced axon degeneration and suggest that targeting cADPR signaling provides a potential therapeutic approach for treating paclitaxel-induced peripheral neuropathy (PIPN).**

## Introduction

Axons provide critical long-distance connections among neurons. Functional and structural defects in these connections, known as axonopathy, are a hallmark of many central and peripheral neurodegenerative diseases. Toxins, disease, or injury can all initiate local signaling cascades, leading to dysfunction and destruction of the affected axons. Axon degeneration often begins at axon terminals and progresses in a retrograde direction toward the neuron cell bodies, a process known as “dying-back” degeneration (Wang et al., 2012). Dying-back axon degeneration is a key pathological feature observed in cancer patients suffering from chemotherapy-induced peripheral neuropathy (CIPN; Fukuda et al., 2017). The most common manifestations of CIPN are excess pain and deficits of sensation in a stocking and glove distribution, in which the distal limbs are most significantly affected (Schneider et al., 2015; Seretny et al., 2014). Although CIPN is often reversible over time, a significant fraction of patients develop long-lasting, untreatable pain and

severe sensory deficits persisting for years after the cessation of cancer treatment (Dorsey et al., 2019). Defective axonal transport, mitochondrial dysfunction, and intra-axonal calcium dysregulation have all been implicated as key events in the process of chemotherapy-induced axon degeneration (Berbusse et al., 2016; Bobylev et al., 2015; Boehmerle et al., 2007; Pease-Raissi et al., 2017). However, it remains unclear how these processes coordinate with one another to cause degeneration. Given the lack of understanding of the underlying mechanisms, it is not surprising that there are no effective treatments available for CIPN. Methods of mitigating CIPN are currently limited to dose reduction or early termination of chemotherapy, which compromises the therapeutic response and patient survival (Dorsey et al., 2019). Thus, there is an urgent need for improved understanding of CIPN mechanisms and discovery of effective therapeutic targets.

Recent insights into the mechanism of axon degeneration caused by physical injury provide important clues for understanding axon

<sup>1</sup>Department of Neurobiology, Harvard Medical School, Boston, MA; <sup>2</sup>Department of Cancer Biology, Dana-Farber Cancer Institute, Boston, MA; <sup>3</sup>Metabolomics Innovation Resource, Goodman Cancer Research Centre, McGill University, Montréal, Quebec, Canada; <sup>4</sup>Institute of Molecular Biology, Academia Sinica, Taipei, Taiwan, Republic of China; <sup>5</sup>Department of Biological Chemistry and Molecular Pharmacology, Harvard Medical School, Boston, MA; <sup>6</sup>Broad Institute of Harvard and Massachusetts Institute of Technology, Cambridge, MA; <sup>7</sup>Department of Genetics, Washington University School of Medicine, St. Louis, MO; <sup>8</sup>Department of Developmental Biology, Washington University School of Medicine, St. Louis, MO; <sup>9</sup>Needleman Center for Neurometabolism and Axonal Therapeutics, Washington University School of Medicine, St. Louis, MO.

Correspondence to Rosalind A. Segal: [rosalind\\_segal@dfci.harvard.edu](mailto:rosalind_segal@dfci.harvard.edu).

© 2021 Li et al. This article is distributed under the terms of an Attribution-Noncommercial-Share Alike-No Mirror Sites license for the first six months after the publication date (see <http://www.rupress.org/terms/>). After six months it is available under a Creative Commons License (Attribution-Noncommercial-Share Alike 4.0 International license, as described at <https://creativecommons.org/licenses/by-nc-sa/4.0/>).

degeneration due to chemotherapy. Studies of Wallerian degeneration in *Drosophila*, zebrafish, and mammalian models have identified Sterile  $\alpha$  and Toll/Interleukin-1 Receptor (TIR) motif-containing 1 (Sarm1) as a key mediator of injury-induced axonal degeneration (Gerdtz et al., 2015, 2013; Osterloh et al., 2012; Tian et al., 2020). Loss of Sarm1 also protects against diabetes, glaucoma, and chemotherapy-induced neuropathy (Cetinkaya-Fisgin et al., 2020; Geisler et al., 2019a, 2016; Ko et al., 2020; Turkiew et al., 2017), suggesting a convergent pathway among axon degeneration induced by injury, chemotherapy, and metabolic disorder. Sarm1 functions as a nicotinamide adenine dinucleotide (NAD) hydrolase, hydrolyzing NAD to generate nicotinamide (NAM), cyclic-ADP Ribose (cADPR), and ADP Ribose (ADPR; Essuman et al., 2017). The catalytic domain of Sarm1 is located in the C-terminal TIR domain (Essuman et al., 2017). Activation of the TIR domain by dimerization is sufficient to trigger axon degeneration (Gerdtz et al., 2015). Conversely, mutations that enzymatically disable Sarm1 prevent axotomy-induced axon degeneration (Essuman et al., 2017; Geisler et al., 2019b; Summers et al., 2016). These findings indicate the NADase activity of Sarm1 is both necessary and sufficient for its pro-degenerative function. The question remains whether Sarm1-dependent axon degeneration is exclusively due to NAD loss and subsequent metabolic catastrophe or whether NAD-derived metabolites such as cADPR and ADPR also contribute to degeneration. Studies of Wallerian degeneration demonstrated that cADPR is a biomarker for Sarm1 activity but does not by itself trigger axon degeneration (Sasaki et al., 2020). A recent study showed that NAD breakdown products signal cell death following TIR domains' activation in plants (Wan et al., 2019), suggesting excess cADPR and ADPR production can contribute to the degenerative process. However, it is not clear whether cADPR may contribute to slowly progressing types of Sarm1-dependent degeneration such as those caused by chemotherapies. cADPR is a calcium-mobilizing agent that potentiates calcium-induced calcium release in sea urchin egg homogenate (Clapper et al., 1987; Lee, 1993, 1989) and in other cell types, including T lymphocytes (Guse et al., 1999), cardiac myocytes (Rakovic et al., 1996), and neurons (Currie et al., 1992; Higashida et al., 2001). Studies using pharmacological approaches or in vitro reconstitution of channels have shown that cADPR modulates intracellular calcium release through ryanodine receptor channels (RyRs) but not inositol 1,4,5-trisphosphate receptors (IP<sub>3</sub>Rs; Clapper et al., 1987; Dargie et al., 1990; Mészáros et al., 1993). Moreover, both cADPR and ADPR activate TRPM2, a calcium-permeable, nonspecific cation channel located predominantly on the plasma membrane (Kolisek et al., 2005; Yu et al., 2019). These observations raise the possibility that cADPR and ADPR, the products of activated Sarm1, may not merely be readouts of Sarm1 but may constitute signaling molecules that contribute to axonal calcium dysregulation and degeneration.

Axotomy rapidly induces increased axonal calcium flux (Adalbert et al., 2012; Loreto et al., 2015; Vargas et al., 2015), and both extracellular and intracellular calcium stores are involved (Villegas et al., 2014). Paclitaxel and vincristine, two microtubule-targeting chemo-drugs, alter ATP-induced calcium release in

neuroblastoma cells and dorsal root ganglion (DRG) primary cultures (Benbow et al., 2012; Boehmerle et al., 2007; Pease-Raissi et al., 2017), while depletion of calcium channels or inhibition of calpain, a calcium-dependent protease, prevents paclitaxel-induced axon degeneration (Pease-Raissi et al., 2017; Wang et al., 2004). These data collectively identify calcium dysregulation as a key component of axon degeneration induced by both chemotherapy and injury. However, current studies lack direct observation of calcium changes within axons following chemotherapy drug treatment and have not identified the sources of calcium that contribute to degeneration.

Here, we directly visualized intra-axonal calcium changes following paclitaxel treatment using GCaMP6s targeted to axons of sensory neurons in microfluidic chambers. We found that paclitaxel leads to Sarm1 activation and excess cADPR production, which contributes to paclitaxel-induced intra-axonal calcium flux and degeneration. We found that interference with cADPR signaling using genetic or pharmacologic intervention prevents paclitaxel or Sarm1 activation-triggered axonal calcium elevation and degeneration in cultured sensory neurons. Finally, we showed that a cADPR antagonist attenuates paclitaxel-induced neuropathy in vivo without affecting the anti-tumor efficacy of paclitaxel. Our data provide new insights into the molecular mechanisms of paclitaxel-induced peripheral neuropathy and suggest cADPR as a promising therapeutic target for treating paclitaxel-induced peripheral neuropathy.

## Results

### Paclitaxel treatment increases cADPR levels through Sarm1 activation

Local paclitaxel treatment of the axons of sensory neurons in compartmentalized cultures leads to axon degeneration in DRG neurons (Fig. 1 A; Gornstein and Schwarz, 2017; Pease-Raissi et al., 2017; Yang et al., 2009). This axon degeneration was quantified as the ratio of fragmented axons normalized to total axon area (Fig. 1 B). In contrast, paclitaxel-induced axon degeneration was prevented in Sarm1 shRNA-transduced DRG neurons (Fig. 1, A and B; and Fig. S1 D). The efficiency of Sarm1 shRNA was verified at both the mRNA and protein levels (Fig. S1, A and B). This result demonstrates that Sarm1 is required for paclitaxel-induced axon degeneration in a cell autonomous fashion; moreover, the compartmentalized culture system provides a good in vitro model to address the mechanisms of Sarm1-dependent axon degeneration.

As activated, Sarm1 catalyzes the breakdown of NAD and NADP to generate cADPR and ADPR, we asked whether paclitaxel affects NAD and its metabolites. Paclitaxel treatment of DRG sensory neuron cultures significantly decreased NAD and NADP levels as measured via liquid chromatography-tandem mass spectrometry (LC-MS/MS; Fig. 1, D and E). Knockdown of Sarm1 increased baseline NAD levels in vehicle-treated and paclitaxel-treated cultures and restored NAD and NADP levels in paclitaxel-treated cultures to the same level as seen in the untreated control group (Fig. 1, D and E; Table S1; and Table S2). Interestingly, comparing cultures with Sarm1 knockdown that were treated with vehicle and those treated with paclitaxel

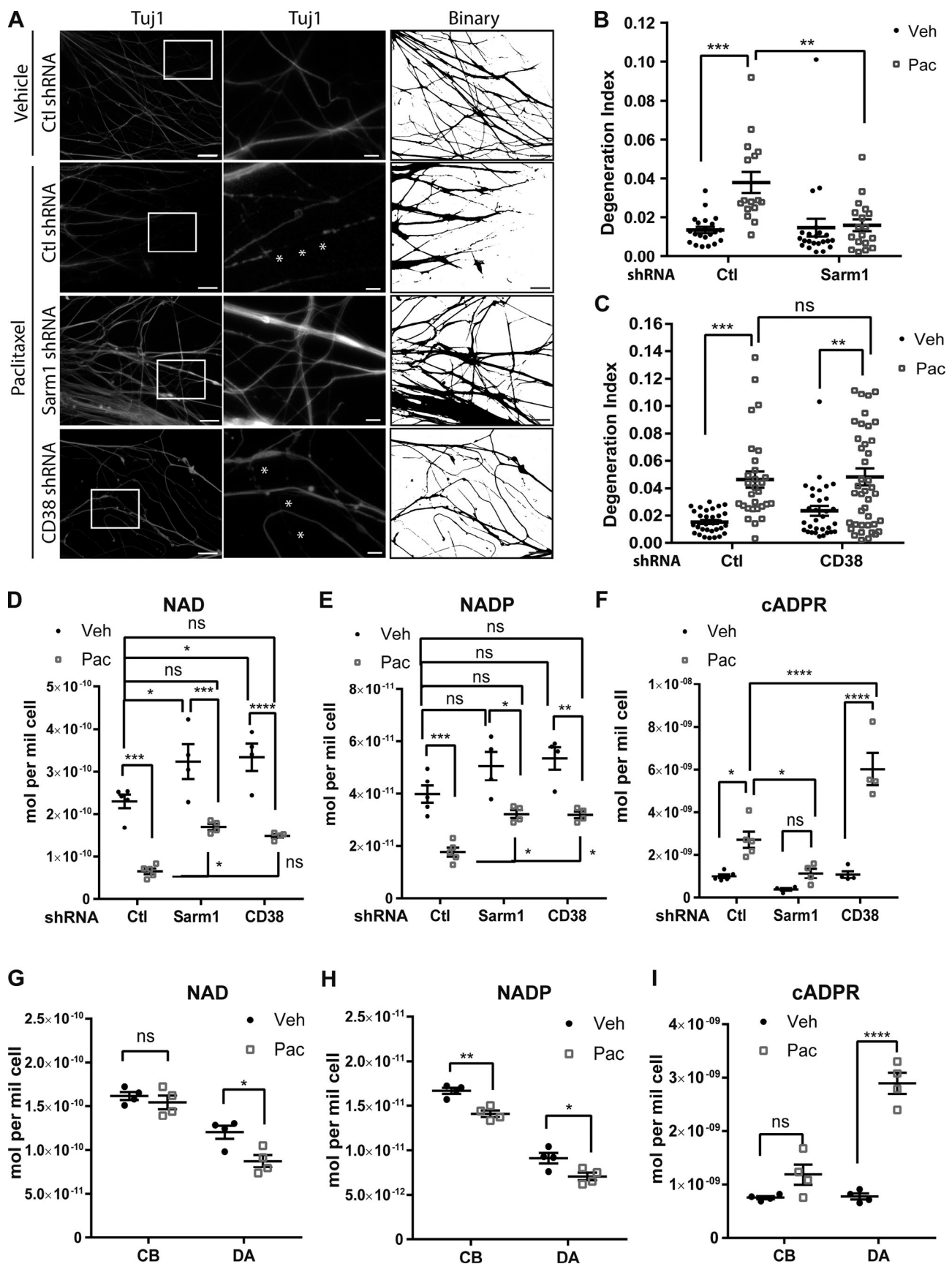


Figure 1. **Paclitaxel-induced cADPR production and axon degeneration require Sarm1 but not CD38.** (A) Tuj1 immunostaining and corresponding binarized images of axon endings of DRG neurons grown in compartmented cultures. Following lentiviral infection with shRNA against Sarm1 or CD38 or control

shRNA (Ctl), 30 nM paclitaxel (Pac) or vehicle control (Veh) was applied to axons for 24 h. White boxes outline regions shown at higher magnification in the center panels. White stars indicate fragmented region of axons displayed as interruptions in Tuj1 continuity. Scale bar: 20  $\mu$ m (left and right panels), 50  $\mu$ m (middle insets). See Fig. S1 C for representative images of vehicle-treated axons expressing Sarm1 or CD38 shRNA. **(B and C)** Quantification of the degeneration index of A in DRG neurons with Sarm1 knockdown (B) and CD38 knockdown (C): ratio of area of fragmented axons to total axon area (degeneration index). Data represent mean  $\pm$  SEM; individual data points are shown. N represents number of images. Data are pooled from three (B) and five (C) independent experiments. \*\*,  $P < 0.01$ ; \*\*\*,  $P < 0.001$  by two-way ANOVA with Tukey's multiple comparisons test. **(D–F)** Level of NAD (D), NADP (E), and cADPR (F) in DRG neurons cultured for 24 h with 600 nM paclitaxel (Pac) or DMSO (Veh) following lentiviral infection with shRNA to Sarm1 or CD38 or control shRNA. Data represent mean  $\pm$  SEM; individual data points are shown. N represents number of independent experiments. \*,  $P < 0.05$ ; \*\*,  $P < 0.01$ ; \*\*\*,  $P < 0.001$ ; \*\*\*\*,  $P < 0.0001$  by two-way ANOVA with Tukey's multiple comparison test. **(G–I)** Levels of NAD (G), NADP (H), and cADPR (I) in distal axons (DA) and cell bodies (CB) of DRG neurons after 24 h of 30 nM paclitaxel (Pac) or DMSO (Veh) applied to axons. Data represent mean  $\pm$  SEM; individual data points are shown. N represents number of independent experiments. \*,  $P < 0.05$ ; \*\*,  $P < 0.01$ ; \*\*\*\*,  $P < 0.0001$ ; two-way ANOVA, Tukey's multiple comparisons test.

showed that paclitaxel still significantly decreased NAD and NADP in these Sarm1-depleted DRG neurons (Fig. 1, D and E; Table S1; and Table S2). Paclitaxel treatment also significantly increased cADPR levels (Fig. 1 F and Table S3), the product of NAD hydrolysis and a validated biomarker of SARM1 activity (Sasaki et al., 2020). Sarm1 depletion inhibited paclitaxel-induced cADPR production and restored cADPR to the same level as seen in the untreated control group (Fig. 1 F and Table S3). In contrast to NAD and NADP levels, paclitaxel does not cause any significant increase of cADPR in Sarm1-depleted DRG neurons.

We asked how these metabolic changes contribute to paclitaxel-induced axon degeneration. One possibility is that excess NAD and NADP consumption leads to insufficient energy supply and axon maintenance failure, thereby triggering degeneration. To investigate whether the absolute levels of NAD and NADP are critical for paclitaxel-induced axon degeneration, we tested the neuroprotective effect of CD38, another NADase (Aksoy et al., 2006). Similar to Sarm1, knockdown of CD38 increases the NAD levels in both vehicle- and paclitaxel-treated cultures, which restored NAD and NADP in paclitaxel-treated cultures to the levels seen in the vehicle-treated control cultures (Fig. 1, D and E; and Fig. S1 C). As seen for Sarm1 knockdown, comparing cultures with CD38 knockdown that were treated with vehicle and those treated with paclitaxel showed that paclitaxel still significantly decreases NAD and NADP in these CD38-depleted DRG neurons. However, unlike Sarm1 depletion, CD38 depletion failed to block paclitaxel-induced degeneration (Fig. 1, A and C; and Fig. S1 D). This result is consistent with the previous finding that murine CD38<sup>-/-</sup> neurons were not protected from axotomy (Sasaki et al., 2009). These data collectively suggest that neither the absolute levels nor the relative reduction of NAD and NADP is a critical determinant of paclitaxel-induced axon degeneration.

Surprisingly, rather than inhibiting cADPR production, CD38-deficient DRG neurons showed enhanced cADPR elevation when treated with paclitaxel (Fig. 1 F). This was a synergistic effect with paclitaxel, as CD38 depletion alone did not alter basal levels of cADPR (Fig. 1 F). Since CD38 functions as both an NADase and a cADPR hydrolase (Chini, 2009), it is possible that excess cADPR produced by paclitaxel-induced Sarm1 activity accumulates further upon CD38 deficiency. The differential effects of Sarm1 and CD38 on cADPR production raise the possibility that cADPR itself contributes to paclitaxel-induced degeneration.

We then evaluated the subcellular localization of paclitaxel-induced metabolites using sensory neurons in the compartmentalized culture systems. Axonal treatment with paclitaxel

significantly increased cADPR levels in distal axons but not in cell bodies (Fig. 1 I), while NAD and NADP levels showed small decreases in both distal axons and cell bodies (Fig. 1, G and H). We also found that ADPR, the other breakdown component of NAD, was not affected by paclitaxel in either cell bodies or distal axons (Fig. S1 E). These results demonstrate that the local accumulation of cADPR in axons correlates with paclitaxel-induced axon degeneration.

### Paclitaxel leads to Sarm1-dependent axonal calcium flux

Calcium dysregulation is a critical step in the process of axon degeneration. However, there is no direct evidence showing paclitaxel changes axonal calcium flux. As cADPR can potentiate calcium release from intracellular stores (Clapper et al., 1987; Lee et al., 1989), the paclitaxel-induced increase in cADPR in distal axons could alter intra-axonal calcium flux. To monitor axonal calcium alterations in space and time, we cultured DRG neurons in microfluidics and transduced the neurons with AAV9-expressing axon-localizing GCaMP6s containing a sequence from GAP-43 that targets the protein to axons, followed by a P2A peptide-linked mRuby3 (AAV9-GCaMP6s-mRuby3; Broussard et al., 2018). This allows us to normalize the calcium GCaMP6s fluorescence to the level of mRuby3 expression within axons at each time point. Simultaneously, we transduced the DRG cells with lentivirus expressing Sarm1 shRNA or Turbo-green fluorescent protein (tGFP)-targeted control shRNA. A recent study indicates that changes in substrate may alter the timing and dose responses of paclitaxel-induced axon degeneration (Shin et al., 2021). As the substrate in microfluidic cultures consists of laminin, rather than the Matrigel used in Campenot cultures, we used the higher dose of paclitaxel that is required for degeneration in noncompartmental cultures (600 nM) and causes axon retraction in microfluidic chambers (Fig. S2, A and B). We imaged GCaMP6s and mRuby3 signals at multiple time points in the same location over the course of 48 h of paclitaxel or vehicle treatment. At each time point, the GCaMP6s signal was normalized to mRuby3 signal (GCaMP6s/mRuby3), and this ratio was then normalized to GCaMP6s/mRuby3 at time 0 [(GCaMP6s/mRuby3)<sub>0</sub>]. We found that paclitaxel gradually increases axonal calcium signal (Fig. 2, A and B), and this is followed by axon degeneration (Fig. S2 C, white arrowheads).

In sensory neurons, knockdown of Sarm1 prevented paclitaxel-induced axonal calcium elevation (Fig. 2, A and B; and Fig. S2 C), indicating that Sarm1 is required for paclitaxel-induced axonal calcium flux. As CD38 depletion enhances the increase in cADPR



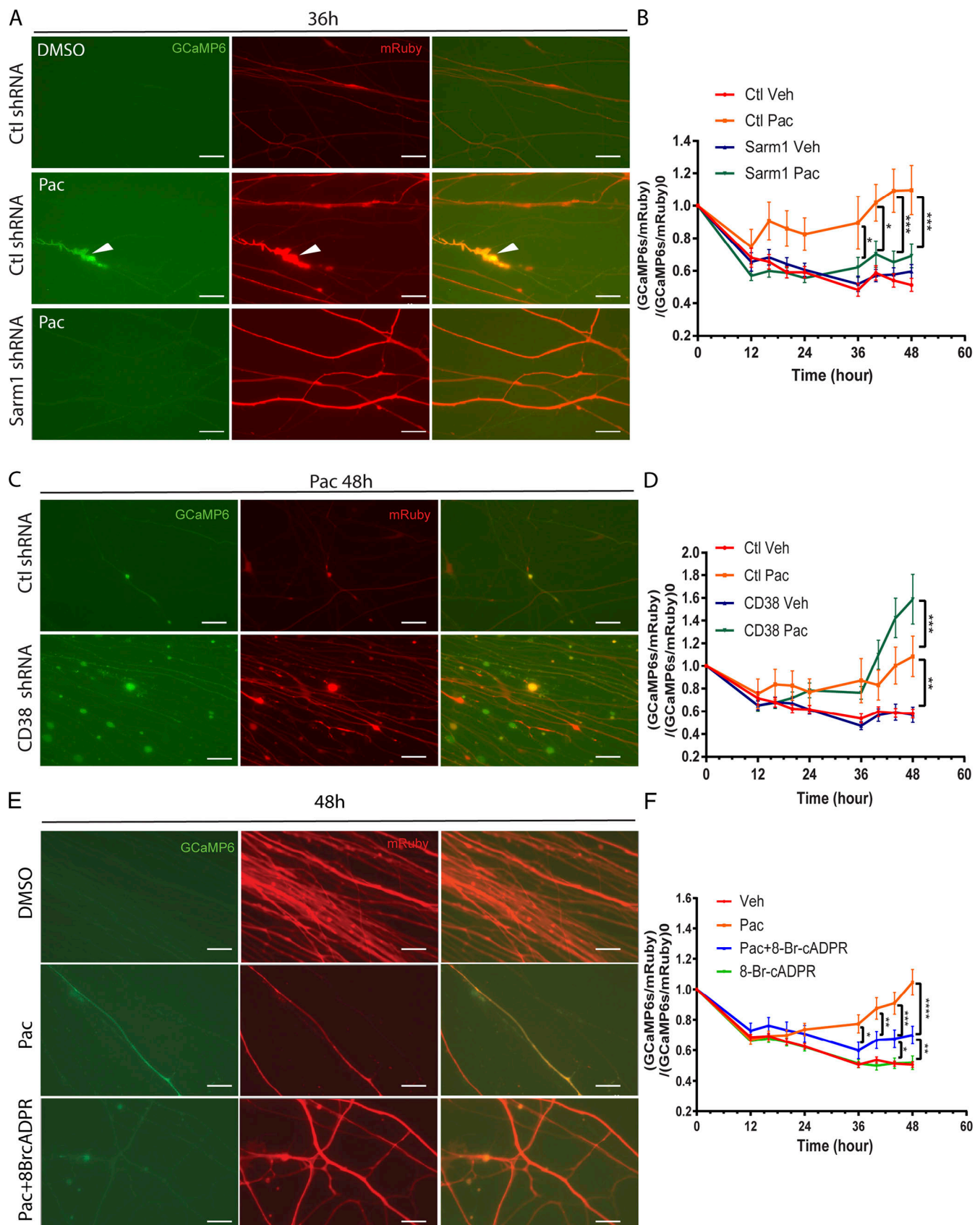


Figure 2. **Paclitaxel leads to Sarm1-dependent increase in axonal calcium.** (A and C) Representative images of GCaMP6s (green) and mRuby3 (red) in axons of DRG neurons also expressing indicated shRNA at 36 h (A) and 48 h (C) after 600 nM paclitaxel (Pac) or vehicle control (Veh) was applied to axons. White arrowhead indicates axon with elevated calcium signal. This axon later degenerates (also see Fig. S2 A). Scale bar: 20  $\mu$ m. (B and D) Quantification of

calcium signal calculated as  $(\text{GCaMP6s}/\text{mRuby3})/(\text{GCaMP6s}/\text{mRuby3})_0$ .  $(\text{GCaMP6s}/\text{mRuby3})$  represents calcium signal at each time point, and  $(\text{GCaMP6s}/\text{mRuby3})_0$  represents calcium signal at time 0 before treatment. Data represent mean  $\pm$  SEM. N represents number of images. 8–10 images from each sample per experiment; one or two samples per condition per experiment. Data pooled from four independent experiments. Three experiments from D share the same control shRNA samples with B. \*,  $P < 0.05$ ; \*\*,  $P < 0.01$ ; \*\*\*,  $P < 0.001$ ; by two-way ANOVA with Tukey's multiple comparisons test for each time point. **(E)** Representative images of GCaMP6s (green) and mRuby3 (red) of DRG axons treated with DMSO, 600 nM paclitaxel alone, or 600 nM paclitaxel with 20  $\mu\text{M}$  8-Br-cADPR. Scale bar: 20  $\mu\text{m}$ . **(F)** Quantification of calcium signal of DRG axons treated with DMSO, 600 nM paclitaxel, 600 nM paclitaxel with 20  $\mu\text{M}$  8-Br-cADPR, or 20  $\mu\text{M}$  8-Br-cADPR. Data represent mean  $\pm$  SEM. N represents number of images. 8–10 images for each sample per experiment. Data pooled from 14 independent experiments. \*,  $P < 0.05$ ; \*\*,  $P < 0.01$ ; \*\*\*,  $P < 0.001$ ; \*\*\*\*,  $P < 0.0001$  by two-way ANOVA with Tukey's multiple comparisons test for each time point. Ctl, control.

levels induced by paclitaxel, we also examined the calcium signal in CD38-depleted cultures. In direct contrast to Sarm1 knockdown, CD38 knockdown further increased axonal calcium levels in axons treated with paclitaxel without altering calcium signals in axons treated with vehicle control (Fig. 2, C and D). Thus, the results observed with calcium imaging closely parallel the enhanced cADPR level that is seen in paclitaxel-treated, but not vehicle-treated, CD38-depleted neurons. These results indicate that changes in cADPR correlate well with axonal calcium levels and that levels or dynamic changes of NAD and NADP do not show this correlation.

To determine whether cADPR itself contributes to paclitaxel-induced axonal calcium flux, we tested the effects of 8-Br-cADPR, a cell-permeable antagonist of cADPR, which blocks cADPR-induced calcium release in sea urchin egg homogenate (Walseth and Lee, 1993) as well as in astrocytes and bone marrow neutrophils (Banerjee et al., 2008; Partida-Sanchez et al., 2007). We found that treatment with 8-Br-cADPR together with paclitaxel in axons partially decreased the axonal calcium flux compared with axons treated with paclitaxel alone (Fig. 2, E and F), suggesting cADPR is one of the factors that contributes to paclitaxel-triggered calcium flux.

### Sarm1 activation triggers axonal calcium flux

We then asked whether Sarm1 activation is not only necessary but is also sufficient to increase axonal calcium flux. We transduced DRG neurons with AAV9-GCaMP6s-mRuby3 together with lentivirus expressing the Sarm1 TIR domain (sTIR) linked to FkbpF36V, so homodimerization and enzymatic activation of the Sarm1 NADase can be triggered upon addition of B/B homodimerizer (FkbpF36V; Gerdts et al., 2015; see Fig. S3 A for illustration). Dimerization of this TIR domain activates the enzyme, generating cADPR (Fig. 3 A), and causes axon degeneration within 2–6 h (Gerdts et al., 2015). Axonal calcium signals started to increase  $\sim 2$  h after B/B homodimerizer was added to the axon chamber, and signal continued to increase throughout the 4-h time window (Fig. 3, B and C). As a control, dimerization of FkbpF36V-tagged MYD88 TIR domain (mTIR), which does not possess NADase activity or induce axon degeneration (Gerdts et al., 2015), failed to trigger intra-axonal calcium elevation (Fig. 3, B and C). These data together indicate that Sarm1 is necessary and sufficient for axonal calcium elevation. We found that axonal treatment with 8-Br-cADPR partially inhibited axonal calcium elevation caused by sTIR dimerization (Fig. 3, B and C). We tested a second cADPR antagonist, 8-Br-7-CH-cADPR, which similarly showed partial inhibition of calcium elevation caused by sTIR dimerization (Fig. 3 D). The partial rescue by

cADPR antagonists indicates that cADPR contributes to calcium modulation in axons, but it is not the only factor that is involved in the calcium flux initiated by paclitaxel treatment or by Sarm1 activation. cADPR is known to modulate calcium release in a calcium-induced calcium release manner (Gallione et al., 1991), and our data are consistent with a model in which cADPR functions as a calcium modulator that enhances calcium release and synergizes with other factors (Gallione and White, 1994) to induce axon degeneration.

### cADPR antagonists are neuroprotective in vitro

To investigate this model and determine whether cADPR-dependent calcium mobilization contributes to axon degeneration downstream of paclitaxel, we tested the neuroprotective effect of 8-Br-cADPR in compartmentalized cultures. Axonal treatment with 8-Br-cADPR significantly decreased paclitaxel-induced degeneration in a concentration-dependent manner (Fig. 4, A and B). We also tested the more potent cADPR antagonist 8-Br-7-CH-cADPR (Moreau et al., 2011). Axonal treatment with 8-Br-7-CH-cADPR significantly decreased paclitaxel-induced degeneration at concentrations as low as 0.1  $\mu\text{M}$  (Fig. 4 C), further implicating cADPR in paclitaxel-induced axon degeneration. One alternative explanation of our results is that 8-Br-cADPR could function as a direct inhibitor of Sarm1 and thereby suppress cADPR production. An in vitro Sarm1 activity assay using purified Sarm1 protein supplemented with NAD and nicotinamide mononucleotide (NMN) demonstrated that 8-Br-cADPR did not affect Sarm1 NADase activity as assayed by the production of ADPR or Nam (Fig. 4, D and E). Moreover, axonal treatment with 8-Br-cADPR did not alter sTIR dimerization-induced cADPR production (Fig. 3 A), indicating that the neuroprotective effect of 8-Br-cADPR is downstream of Sarm1.

One discrepancy we noticed is that 8-Br-cADPR only partially inhibited paclitaxel or Sarm1 activation-induced axonal calcium flux but rescued the degeneration index completely to the baseline level. This can be explained by technical differences in the systems, timing, and paclitaxel concentrations used for calcium imaging versus axon degeneration assay. Sarm1 depletion, as shown above, completely inhibited paclitaxel-induced calcium flux and degeneration. To compare the neuroprotective effects of Sarm1 depletion and inhibition of cADPR signaling, we evaluated axon degeneration after various times of paclitaxel treatment. We found that 8-Br-cADPR and knockdown of Sarm1 showed similar neuroprotection at 24 h of paclitaxel treatment. Sarm1 depletion continued to show full protection 36 h after paclitaxel treatment, at which time 8-Br-cADPR only partially rescued the degeneration (Fig. S3 B), suggesting cADPR may be

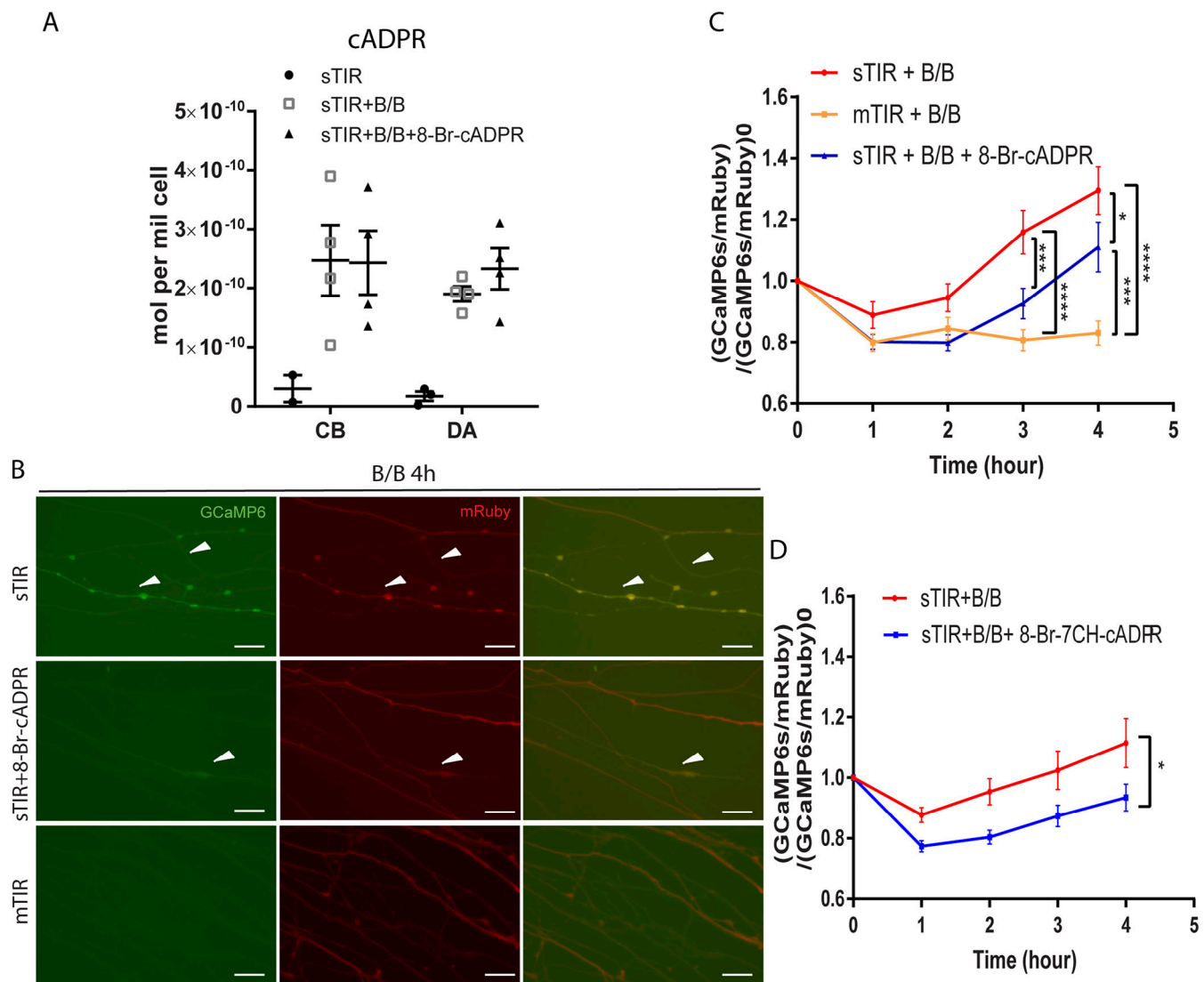


**Figure 3. Sarm1 activation triggers axonal calcium flux partially through cADPR.** (A) Level of cADPR in cell bodies (CB) and distal axons (DA) from compartmentalized cultures after 3 h of 50 nM B/B homodimerizer, 50 nM B/B homodimerizer together with 10  $\mu$ M 8-Br-cADPR, or vehicle added to axons following infection with lentivirus expressing FkbpF36V-sTIR. Data represent mean  $\pm$  SEM; individual data points are shown. N represents four independent experiments. For two samples of vehicle-treated cell bodies (CB) and one of distal axons (DA), no cADPR was detected. These data points are not shown. (B) Representative images of GCaMP6s (green) and mRuby3 (red) of axons of DRG neurons expressing FkbpF36V-sTIR (top and middle) or FkbpF36V-mTIR (bottom) 4 h after axonal treatment of 50 nM B/B homodimerizer together with 10  $\mu$ M 8-Br-cADPR (middle) or saline (top and bottom). Arrowheads indicate calcium elevated axons. Scale bar: 20  $\mu$ m. (C) Quantification of calcium signal of B calculated as  $(\text{GCaMP6s}/\text{mRuby})/(\text{GCaMP6s}/\text{mRuby})_0$ . (GCaMP6s/mRuby) represents calcium signal at each time point, and  $(\text{GCaMP6s}/\text{mRuby})_0$  represents calcium signal at time 0 before treatment. Data represent mean  $\pm$  SEM. N represents number of images. Eight images from each sample per experiment; two replicates per condition. Data pooled from four independent experiments. \*,  $P < 0.05$ ; \*\*\*,  $P < 0.001$ ; \*\*\*\*,  $P < 0.0001$  by two-way ANOVA with Tukey's multiple comparisons test for each time point. (D) Quantification of calcium signal of axons expressing FkbpF36V-sTIR before and after axonal treatment of 50 nM B/B homodimerizer alone or together with 10  $\mu$ M 8-Br-7CH-cADPR. Data represent mean  $\pm$  SEM. N represents number of images. Eight images from each sample per experiment; one or two replicates per condition per experiment. Data pooled from five independent experiments. \*,  $P < 0.05$  by two-way ANOVA with Tukey's multiple comparisons test for each time point.

one of multiple factors that mediate the axon-destructive effects of Sarm1 upon paclitaxel treatment. These results collectively demonstrate that cADPR-dependent calcium signaling contributes to paclitaxel-induced axon degeneration in vitro.

#### cADPR-targeted calcium channels are required for paclitaxel-induced axon degeneration

cADPR modulates intracellular calcium release through intracellular RyRs on the ER (Galione et al., 1991; Guse, 1999;

Mészáros et al., 1993; Sonnleitner et al., 1998). As RyR3 is the major type of RyR in DRG neurons (Lokuta et al., 2002), we knocked down RyR3 using lentivirus-delivered shRNA (Fig. S4 A) and found that RyR3 depletion inhibited paclitaxel-induced axon degeneration (Fig. 5, A and B). These data indicate that RyR3-dependent calcium release from the ER contributes to paclitaxel-induced degeneration. cADPR also directly binds to and activates TRPM2, a calcium-permeable, nonselective cation channel predominantly localized on the plasma membrane



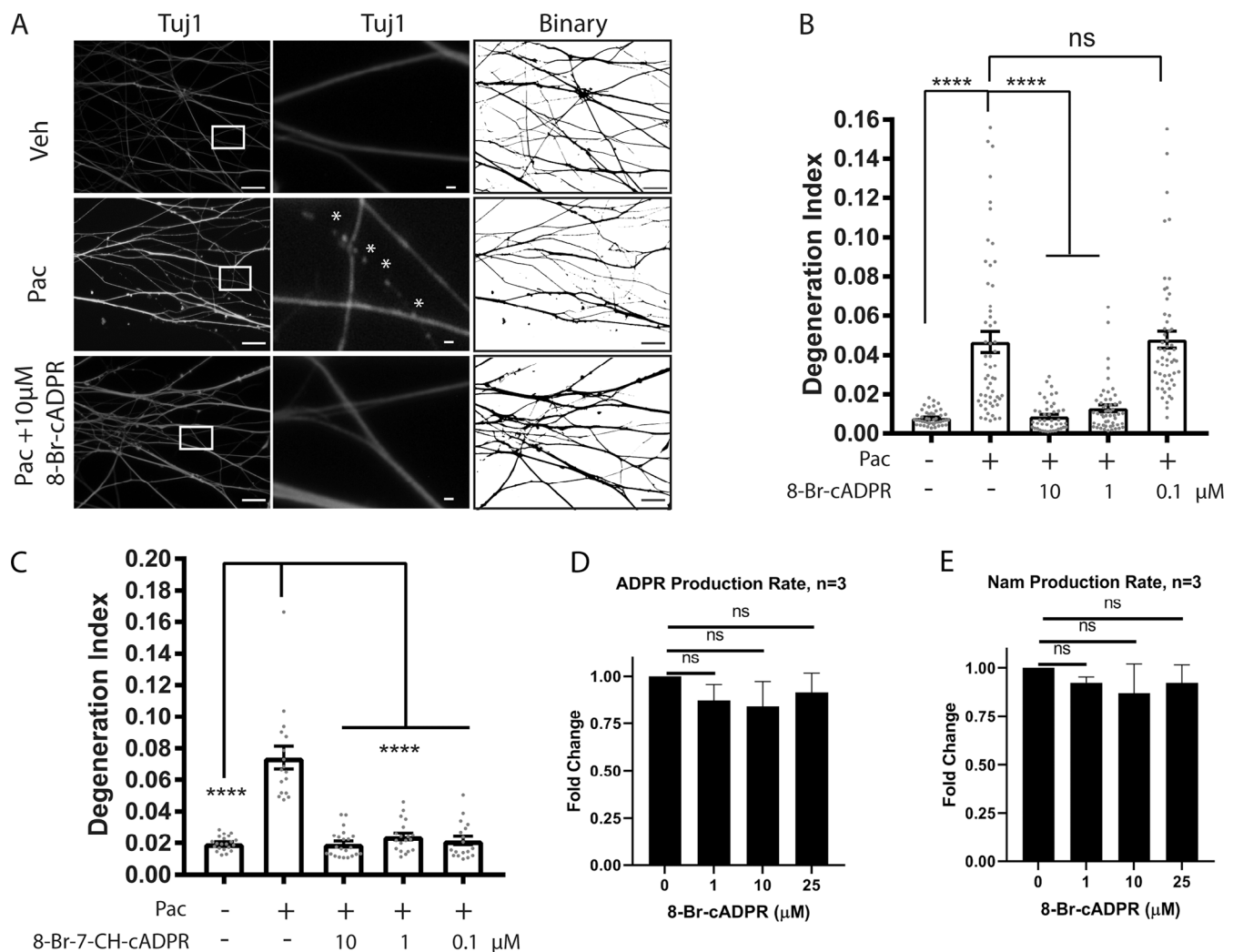


**Figure 4. Paclitaxel-induced axon degeneration is cADPR dependent.** (A) Tuj1 immunostaining and corresponding binarized images of axons in compartmentalized cultures after 24 h of 30 nM paclitaxel (Pac), 30 nM paclitaxel with 10 μM 8-Br-cADPR, or DMSO (Veh) added to axons. White boxes outline regions shown at higher magnification in the center panels. White stars indicate fragmented region of axons displayed as interruptions in Tuj1 continuity. Scale bar: 20 μm (left and right panels), 50 μm (middle insets). (B) Degeneration index of A. Data represent mean ± SEM; individual data points are shown. N represents number of images. Data pooled from 10 independent experiments. \*\*\*\*,  $P < 0.0001$  by one-way ANOVA with Tukey's multiple comparisons tests. (C) Degeneration index of DRG axons after 24 h of DMSO (Veh) or 30 nM paclitaxel (Pac) with indicated concentrations of 8-Br-7-CH-cADPR. \*\*\*\*,  $P < 0.0001$  by one-way ANOVA with Tukey's multiple comparison tests. Data represent mean ± SEM. Individual data points are shown. N represents number of images. Data pooled from three independent experiments. (D and E) Production rate of ADPR (D) and Nam (E) using purified Sarm1 protein supplemented with NAD and NMN together with indicated dosages of 8-Br-cADPR. Data represent mean ± SEM. Data pooled from three independent experiments.

(Kolisek et al., 2005; Yu et al., 2019). Knockdown of TRPM2 also protects against paclitaxel-induced axon degeneration in DRG cultures (Fig. 5, A and B; and Fig. S4 B). These results suggest that calcium release from both intra- and extracellular sources are required for axon degeneration downstream of paclitaxel.

To test whether RyR3 and TRPM2 open in response to activation of Sarm1, we coexpressed FkbpF36V-sTIR and shRNA targeting RyR3 or TRPM2 individually in DRG neurons. Knockdown of RyR3 or TRPM2 individually inhibited axon degeneration caused by sTIR dimerization (Fig. 5, C–E). In control studies, dimerization of FkbpF36V-mTIR did not lead to axon degeneration (Fig. S4 C). While cADPR-dependent calcium mobilization is known to be IP<sub>3</sub>R independent, knockdown of IP<sub>3</sub>R1 also suppressed axon degeneration caused by FkbpF36V-sTIR

dimerization (Fig. 5 D and Fig. S4 D). Together these results suggest that calcium signaling pathways independent of cADPR also contribute to Sarm1 activation-induced degeneration, consistent with the idea that cADPR synergizes with other factors to modulate calcium release and cause degeneration. These data also indicate that both ER calcium stores and extracellular calcium are required for paclitaxel-induced intra-axonal calcium influx and the ensuing axon degeneration.

Sarm1 activation also produces ADPR, the hydrolyzed form of cADPR. Up to 20% of commercially available 8-Br-cADPR may consist of 8-Br-ADPR, an antagonist of ADPR (Walseth, T., personal communication). As ADPR is a more potent ligand for TRPM2 than cADPR (Huang et al., 2018; Kolisek et al., 2005; Yu et al., 2019), we asked whether both components may contribute



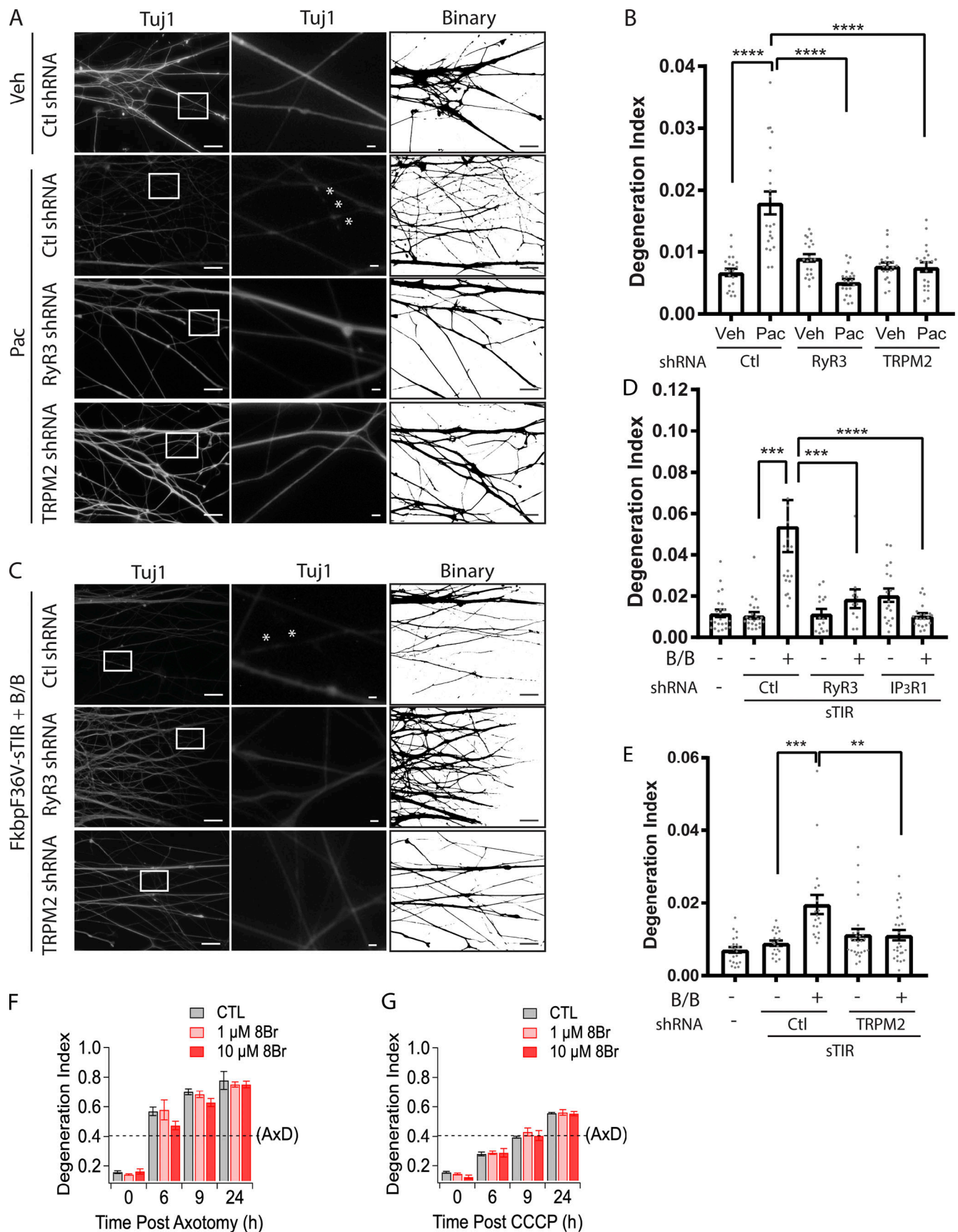


Figure 5. **Paclitaxel-induced axon degeneration requires both ER and extracellular calcium stores.** (A) Tuj1 immunostaining and corresponding binarized images of axons after 24 h of 30 nM paclitaxel (Pac) or DMSO (Veh) added to axons following lentiviral infection with RyR3 or TRPM2 or control shRNA (Ctl).

White boxes outline regions shown at higher magnification in the center panels. White stars indicate fragmented region of axons displayed as interruptions in Tuj1 continuity. Scale bar: 20  $\mu$ m (left and right panels), 50  $\mu$ m (middle insets). **(B)** Degeneration index of A. Data represent mean  $\pm$  SEM. Individual data points are shown. N represents number of images. Data pooled from three independent experiments. \*\*\*\*,  $P < 0.0001$  by one-way ANOVA with Tukey's multiple comparisons tests. **(C)** Tuj1 immunostaining and corresponding binarized images of axons of DRG neurons coexpressing FkbpF36V-sTIR and indicated shRNA, 3 h after 50 nM B/B homodimerizer added to axons. White boxes outline regions shown at higher magnification in the center panels. White stars indicate fragmented region of axons displayed as interruptions in Tuj1 continuity. Scale bar: 20  $\mu$ m (left and right panels), 50  $\mu$ m (middle insets). **(D and E)** Degeneration index of C. Data represent mean  $\pm$  SEM. Individual data points are shown. N represents number of images. Data pooled from three independent experiments. Two data points 0.199 and 0.208 of Ctl + sTIR + B/B that fall outside y axis limit not shown in F. \*\*,  $P < 0.01$ ; \*\*\*,  $P < 0.001$ ; \*\*\*\*,  $P < 0.0001$  by one-way ANOVA with Tukey's multiple comparisons test. **(F and G)** Degeneration index of DRG axons before and 6, 9, and 24 h after axotomy (F) or carbonyl cyanide m-chlorophenylhydrazone (CCCP) treatment (G). \*\*\*\*,  $P < 0.0001$  by one-way ANOVA with Tukey's multiple comparisons tests. Data represent mean  $\pm$  SEM. N represents number of images. Data pooled from three independent experiments. Axd, axon degeneration.

to the observed efficacy. We treated DRG axons with 8-Br-ADPR and found 8-Br-ADPR also decreased paclitaxel-induced axon degeneration (Fig. S4 E), consistent with our finding that TRPM2 and RyR both contribute to paclitaxel-induced degeneration.

Calcium dysregulation is also implicated in Sarm1-dependent axon degeneration in response to physical injury. We asked whether an antagonist of cADPR also protects against Wallerian degeneration. Interestingly, we found 8-Br-cADPR does not prevent axotomy or mitochondrial dysfunction-induced axon degeneration (Fig. 5, F and G). Our data indicate that there are qualitative and/or quantitative differences in the function of cADPR between axon degeneration caused by axotomy and the chemotherapeutic agent paclitaxel.

#### Antagonizing cADPR shows neuroprotective effects against paclitaxel in vivo

Our results indicate that Sarm1 and cADPR are critical for paclitaxel-induced axon degeneration in vitro. To assess the roles of cADPR in paclitaxel-induced peripheral neuropathy in vivo, we treated 2-mo-old C57BL6/J mice with multiple i.p. injections of paclitaxel. Animals were concurrently treated with 8-Br-cADPR or saline control. We then evaluated paclitaxel-induced neuropathy in vivo at both behavioral and pathological levels (Fig. 6 A). A key feature of CIPN in patients is allodynia, a condition in which pain is caused by stimuli that do not normally elicit pain. To assess allodynia in mice before and after paclitaxel, we compared the sensitivity of the mice to mechanical stimuli using filaments of increasing rigidity (Von Frey filament tests). A much smaller force triggered a withdrawal response in animals after paclitaxel treatment compared with pretreatment baseline, while vehicle-treated control mice showed no difference before and after treatment (Fig. 6 B). We found that systemic treatment with 8-Br-cADPR significantly suppressed paclitaxel-induced excess pain sensitivity (Fig. 6 B). Loss of intra-epidermal nerve fiber (IENF) density is a canonical pathological feature of CIPN consistently observed in both patients and animal models (Han and Smith, 2013). We collected skin from the hind paws of the mice after the final behavior test and examined IENF of both thin skin (nondermal papillae-containing plantar metatarsal region) and thick skin (dermal papillae-containing footpad region). Paclitaxel treatment significantly decreased IENF density in both thin (Fig. 6, C and D; and Fig. S5 A) and thick (Fig. 6, C and E; and Fig. S5 B) skin compared with vehicle-treated mice. Treatment with 8-Br-cADPR provided partial protection from paclitaxel-induced

loss of innervation (Fig. 6, C-E; and Fig. S5, A and B). There were no significant body weight changes before and after treatment with either paclitaxel alone or paclitaxel together with 8-Br-cADPR (Fig. S5 C), indicating minimal nonspecific toxicity of these treatments. These results demonstrate a neuroprotective effect of 8-Br-cADPR against paclitaxel-induced peripheral neuropathy in vivo, suggesting that therapies targeting cADPR may be an effective strategy for CIPN.

#### cADPR antagonist does not interfere with paclitaxel's anti-tumor effect

A concern in targeting cADPR for therapeutic purposes is the possibility that this intervention might decrease the anti-neoplastic efficacy of paclitaxel, as calcium homeostasis is also involved in cell cycle regulation and tumor progression (Stewart et al., 2015; Yang et al., 2020). To address this, we used an immunocompetent breast cancer mouse model featuring the breast cancer line E0771 in C57BL6/J mice. We implanted E0771 tumor cells orthotopically into the mammary fat pads of 7-wk-old C57BL6/J mice. We began paclitaxel injections 1 wk after tumor cell injection, when the tumor size reached  $\sim 5$  mm in diameter. To maximize the effect of paclitaxel on tumor growth, paclitaxel or vehicle was injected every other day for a total of eight injections. 8-Br-cADPR or saline was injected after every two paclitaxel or vehicle injections (Fig. 7 A). Tumor sizes increased gradually in mice treated with vehicle + saline up to day 18 (Fig. 7 B), at which point some of these mice approached humane endpoint. Treatment with 8-Br-cADPR alone did not alter tumor growth (Fig. 7 B). Paclitaxel treatment significantly inhibited tumor growth (Fig. 7 B), and combined treatment with paclitaxel + 8-Br-cADPR did not affect the ability of paclitaxel to suppress tumor growth (Fig. 7 B), indicating that 8-Br-cADPR does not interfere with the therapeutic efficacy of paclitaxel. Extended treatment with paclitaxel led to a small but statistically significant weight decrease, while 8-Br-cADPR did not cause weight changes when injected alone or with paclitaxel (Fig. 7 C). We then further analyzed CIPN in these mice by evaluating IENF innervation. IENF density of both thin and thick skins was significantly decreased in paclitaxel-treated mice compared with vehicle control, and 8-Br-cADPR partially but significantly rescued the IENF density loss in both thin and thick skins (Fig. 7, D-F; and Fig. S5, D and E). Notably, 8-Br-cADPR treatment alone did not affect IENF density (Fig. 7, E and F; and Fig. S5, D and E). Together, our data demonstrate that 8-Br-cADPR protects against paclitaxel-induced allodynia

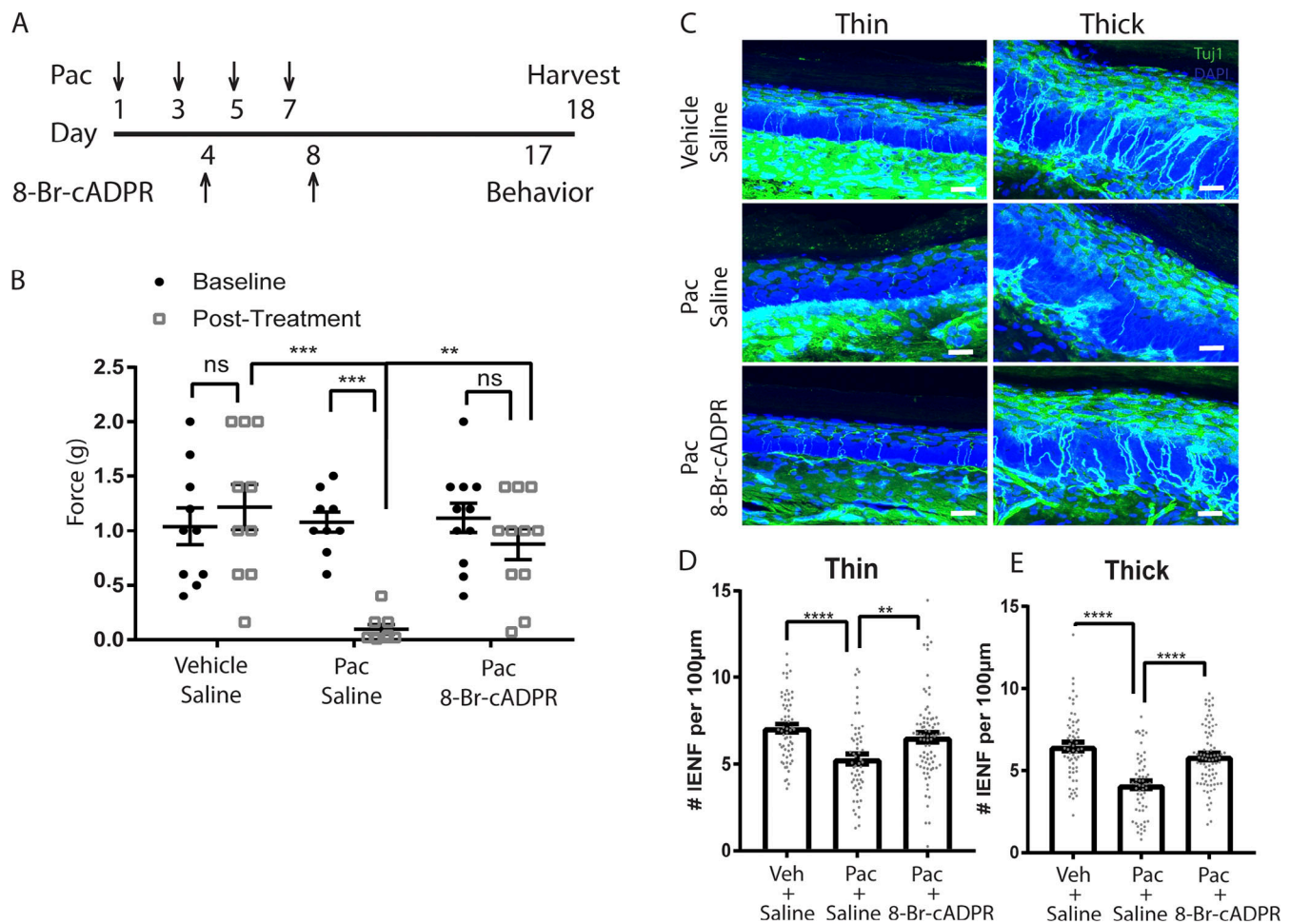


**Figure 6. cADPR antagonist protects against paclitaxel-induced peripheral neuropathy in vivo.** (A) Schematic of experimental design. Paclitaxel (Pac; 20 mg/kg) or vehicle was injected i.p. on days 1, 3, 5, and 7, and 8-Br-cADPR (2 mg/kg) or saline was injected i.p. on days 4 and 8. Final behavior test with Von Frey filaments was performed on day 17, and mice were euthanized for IENF analysis on day 18. (B) Mechanical pain threshold assessments of mice using Von Frey filaments before (Baseline) and 10 d after the final injection (Post-Treatment) of paclitaxel or vehicle control. Data represent mean  $\pm$  SEM; individual data points are shown. N represents number of animals. \*\*,  $P < 0.01$ ; \*\*\*,  $P < 0.001$  by two-way ANOVA with Tukey's multiple comparisons test. (C–E) Quantification and representative images of Tuj1-positive sensory fibers (green) entering the epidermis per 100- $\mu$ m epidermal length in nondermal papillae-containing thin (C, left, and D) and dermal papillae-containing thick (C, right, and E) skin. DAPI counterstain (blue); scale bar: 20  $\mu$ m. \*\*,  $P < 0.01$ ; \*\*\*\*,  $P < 0.0001$  by one-way ANOVA with Tukey's multiple comparisons test. Data represent mean  $\pm$  SEM; individual data points are shown. N represents number of images; 6–10 images from each animal. Animal #: 8, 7, 11 (also see Fig. S5, A and B for statistics based on N = animal #). Veh, vehicle.

and nerve fiber degeneration in vivo without affecting the anti-tumor effect of paclitaxel, indicating it may provide a good therapeutic approach to CIPN.

## Discussion

### cADPR as a calcium modulator in paclitaxel-induced axon degeneration

Understanding the role of calcium dysregulation in chemotherapy-induced axon degeneration requires direct monitoring of axonal calcium flux following drug treatment. In this study, we directly visualized and analyzed axonal calcium flux after paclitaxel treatment and demonstrated that local treatment of paclitaxel causes a progressive increase of axonal calcium, and this precedes axonal degeneration. While previous studies have focused on cADPR as a readout of Sarm1 activity (Sasaki et al., 2020), here we show that cADPR produced by

Sarm1 activity contributes to paclitaxel-induced axonal calcium flux and degeneration. cADPR functions as a modulator of both RyR and TRPM2, and we find that multiple calcium channels, including RyR3, TRPM2, and IP<sub>3</sub>R1, all contribute to axon degeneration initiated by paclitaxel or Sarm1 activation. Thus, multiple intra- and extracellular sources of calcium are involved in axonal calcium flux caused by paclitaxel. A previous study from our laboratory showed that paclitaxel treatment leads to decreased axonal levels of Bclw protein, a Bcl2 family member that binds and regulates IP<sub>3</sub>R1. Thus, paclitaxel both initiates Sarm1-dependent calcium flux and attenuates Bclw-mediated suppression of IP<sub>3</sub>R1-mediated calcium changes. We speculate that cADPR produced by activated Sarm1 together with Bclw depletion both contribute to a complex process of calcium-induced calcium release to promote axon degeneration. Further studies are needed to decipher the initial versus later stages of calcium release in this cascade.



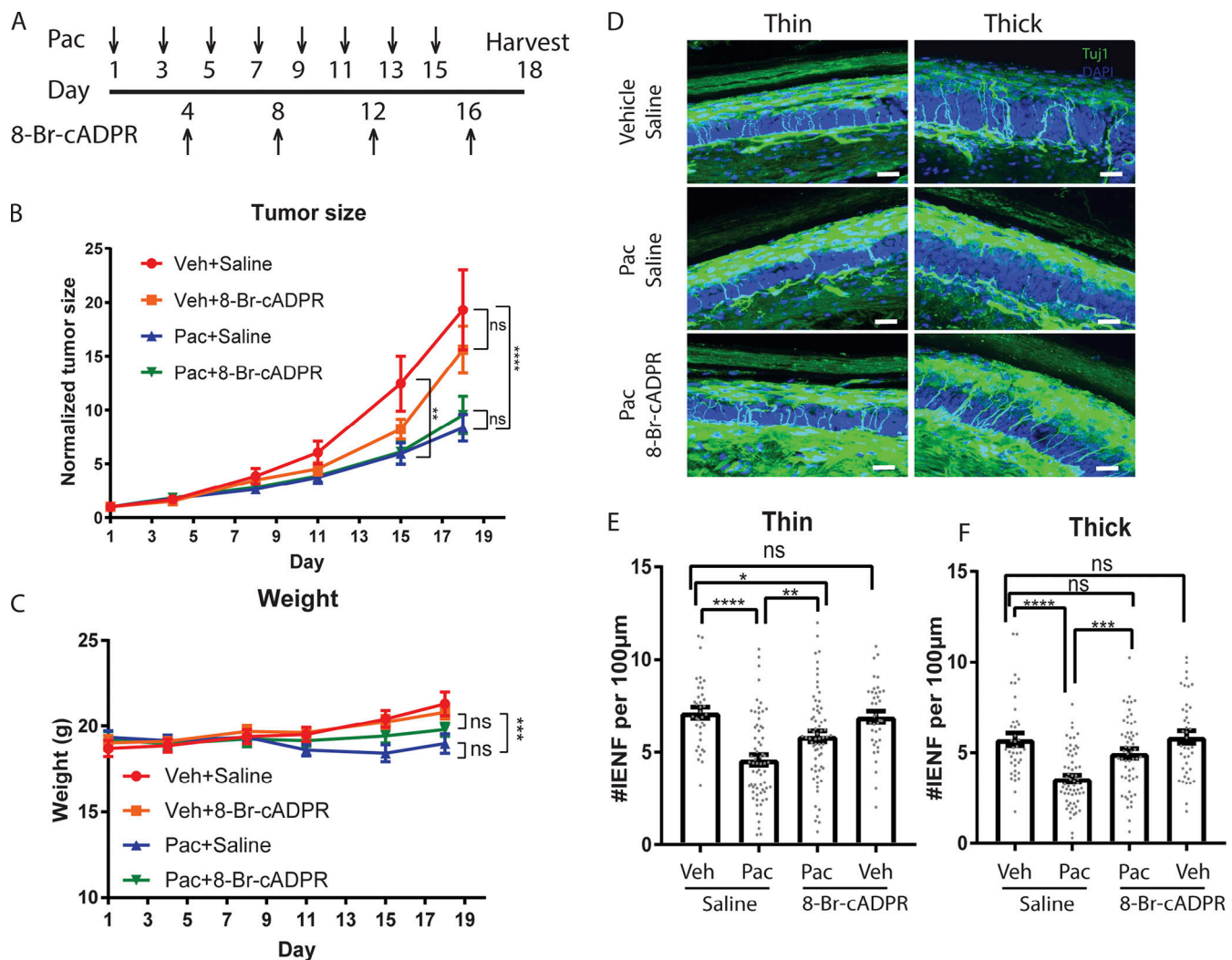


**Figure 7. 8-Br-cADPR does not alter paclitaxel's anti-tumor effect in vivo.** (A) Schematic illustration of experimental design. Paclitaxel (Pac) or vehicle (Veh) was injected i.p. on day 1, 3, 5, 7, 9, 11, 13, and 15, and 8-Br-cADPR or saline was injected i.p. on day 4, 8, 12, and 16. Mice were euthanized for IENF analysis on day 18. (B) Normalized tumor size of mice with E0771 breast cancer cells treated with vehicle + saline, paclitaxel + saline, paclitaxel + 8-Br-cADPR, or vehicle + 8-Br-cADPR. Data represent mean  $\pm$  SEM. N represents number of tumors. Five animals with bilateral tumors were used for each condition. \*\*\*,  $P < 0.001$ ; \*\*\*\*,  $P < 0.0001$  by two-way ANOVA with Tukey's multiple comparisons test at each time point. (C) Body weights of tumor-bearing mice treated with vehicle + saline, paclitaxel + saline, paclitaxel + 8-Br-cADPR, or vehicle + 8-Br-cADPR. Data represent mean  $\pm$  SEM. N represents number of animals. Five animals were used for each condition. \*\*\*,  $P < 0.01$  by two-way ANOVA with Tukey's multiple comparisons tests at each time point. (D–F) Representative images and quantification of Tuj1-positive sensory fibers (green) entering the epidermis per 100- $\mu$ m epidermal length in nondermal papillae-containing thin (D, left, and E) and dermal papillae-containing thick (D, right, and F) skin. DAPI counterstain (blue). Scale bar: 20  $\mu$ m. Data represent mean  $\pm$  SEM; individual data points are shown. N represents number of images, 8–16 images from each animal. Animal# 5, 5, 5 (also see Fig. S5, D and E for statistics based on N = animal #). \*,  $P < 0.05$ ; \*\*,  $P < 0.01$ ; \*\*\*,  $P < 0.001$ ; \*\*\*\*,  $P < 0.0001$  by one-way ANOVA with Tukey's multiple comparisons test.

In contrast to the efficacy of cADPR antagonists in preventing CIPN both in vitro and in vivo, we found that a cADPR antagonist was unable to prevent axotomy-induced axon degeneration. Our data indicate that although axonal degeneration triggered by paclitaxel and axotomy are both Sarm1 dependent, the two signaling cascades are functionally different. This is supported by the fact that paclitaxel causes axonal depletion of Bclw, which leads to IP<sub>3</sub>R1-dependent calcium dysregulation, indicating multiple factors contribute to changes in calcium regulation and the degeneration process in CIPN. Further analyses will be required to identify the mechanisms that differentiate slowly progressing Sarm1-dependent degeneration caused by paclitaxel from the more acute and severe perturbation of axotomy.

#### Sarm1 activation downstream of paclitaxel

The mechanisms that activate Sarm1 are just beginning to be defined. A recent study demonstrates that Sarm1 is a metabolic sensor that can be allosterically regulated by the ratio of NMN and NAD (Figley et al., 2021). Although we do not yet know how paclitaxel activates Sarm1, an attractive idea is that paclitaxel causes defective axon transport of NMNAT2, a highly labile protein that converts NMN to NAD, and must be continuously provided to the axon by fast axonal transport (Gilley and Coleman, 2010). Indeed, depletion of the axon survival factor NMNAT2 leads to Sarm1-dependent axon degeneration (Gilley et al., 2015). We speculate that microtubule-dependent transport

of NMNAT2 may be disrupted by paclitaxel, which leads to NMNAT2 depletion, changes in the ratio of NMN and NAD, and Sarm1 activation. Other molecules, including mitochondrial antiviral signaling protein (MAVS) and syndecan-2 (Sdc2), have been suggested as additional potential regulators of Sarm1 activity (Chen et al., 2011; Mukherjee et al., 2013). Thus, it is also possible that transport of MAVS and/or Sdc2 may be impaired following paclitaxel treatment, leading to changes in axonal MAVS and/or Sdc2 that further activate Sarm1.

### Tumor mouse model in CIPN research and therapeutic implication of cADPR

Our in vivo studies corroborate the involvement of cADPR in paclitaxel-induced peripheral neuropathy. Paclitaxel-treated mice exhibit heightened pain sensitivity and loss of intra-epidermal nerve endings, recapitulating the allodynia and dying-back nerve degeneration observed in patients. I.p. administration of 8-Br-cADPR attenuates paclitaxel-induced peripheral neuropathy both behaviorally and pathologically. The robust protection of 8-Br-cADPR in vivo, however, may involve other components besides the nerve itself, since the role of cADPR as a calcium modulator has also been implicated in the immune system and in glial cells (Banerjee et al., 2008; Guse et al., 1999; Partida-Sánchez et al., 2001). Nevertheless, our results raise the possibility of using cADPR as a potential therapeutic target for treating paclitaxel- and possibly other chemotherapy-induced peripheral neuropathies.

Preventive treatments of CIPN will be given to patients who are undergoing treatment for a malignant cancer. Therefore, in searching for new therapies for CIPN, it is critical that the neuropathic and anti-neoplastic effects of the microtubule-targeting chemo-drugs can be uncoupled from one another. Using an immune competent mouse model of breast cancer, we were able to examine both peripheral neuropathy progression and tumor growth in the same animals. Consistent with prior studies, we found that tumor growth was significantly inhibited by paclitaxel in this model (Bourgeois-Daigneault et al., 2016) and that these paclitaxel-treated mice also exhibited decreased IENF density, confirming that paclitaxel causes peripheral neuropathy in this model. Treatment with the cADPR competitive antagonist 8-Br-cADPR improved the paclitaxel-induced neuropathy without interfering with its anti-tumor effect. Thus, the effects of paclitaxel on cancer growth can potentially be disentangled from its effects on nerve innervation. Our results in vitro and in vivo collectively indicate the potential of targeting cADPR as a novel and promising therapeutic approach for preventing paclitaxel-induced peripheral neuropathy. Further studies investigating the ability of new small-molecule inhibitors of Sarm1 (Hughes et al., 2021) to prevent or delay CIPN in vivo without altering therapeutic effects of chemotherapies may provide additional therapeutic approaches to this major cause of poor quality of life in cancer survivors.

## Materials and methods

Key resources and reagents used in this study are listed in Table S5.

### Mouse line and animal care

All experimental procedures were conducted in accordance with the National Institutes of Health (NIH) guidelines and were approved by the Dana-Farber Cancer Institute or the Washington University School of Medicine, St. Louis Institutional Animal Care and Use Committee.

Timed pregnant Sprague-Dawley rats and CD1 mice were purchased from Charles River. C57BL6/J mice were purchased from The Jackson Laboratory.

### DRG neuron culture

DRGs were dissected from E15 rat embryos, dissociated, and plated in Matrigel (1:45; Thermo Fisher Scientific)-coated p35 dishes, Campenot device, or poly-D-lysine/laminin-coated microfluidic chambers. DRG cultures were maintained in Neuro-Basal medium supplemented with 2% B27, 1% Glutamax, 1% penicillin and streptomycin, 0.08% glucose, 1–100 ng/ml nerve growth factor (NGF)/brain-derived neurotrophic factor (BDNF; PeproTech), and 0.5  $\mu$ M Cytarabine (AraC). Cultures were maintained in incubators at 37°C with 7.5% CO<sub>2</sub>. For non-compartmentalized mass culture, 300,000 cells were plated in each p35 dish. BDNF + NGF was added at a concentration of 100 ng/ml for 2 d and reduced to 10 ng/ml for 5–6 d. Campenot device was prepared as described (Fenstermacher et al., 2015). BDNF + NGF was added to the cell body compartment at a concentration of 10 ng/ml and to the axon compartment at a concentration of 100 ng/ml for 2 d. On day 5, neurotrophins were removed from the cell body compartment and reduced to 1 ng/ml in the axon compartments for 2–3 d. Paclitaxel (30 nM) or DMSO (0.0025%) was added to the axon chambers on days in vitro (DIV) 7–8 for 24 h before fixation. For TIR domain dimerization, 50 nM B/B homodimerizer was added to the axon chambers for 3 h before fixation. For degeneration assay with 8-Br-cADPR treatment, 8-Br-cADPR (0.1–10  $\mu$ M) was added to axon chambers 1 h before paclitaxel or B/B homodimerizer addition and continued to be present in the axon chambers with paclitaxel or B/B homodimerizer until fixation.

Microfluidic chambers (Xona Microfluidics) were prepared according to manufacturer's instruction with laminin and poly-D-Lysine coating. 30,000 neurons were plated in the cell body compartment. BDNF + NGF was added to the cell body compartment at 50 ng/ml and to the axon compartment at 100 ng/ml for 1 d and reduced to 10 ng/ml (cell bodies) and 100 ng/ml (axons) for 1 d and maintained in 5 ng/ml (cell bodies) and 10 ng/ml (axons) for 3–5 d. Paclitaxel (600 nM) or 0.5% DMSO was added to axon compartments on DIV4–5 for 48 h. For TIR domain dimerization, 50 nM B/B homodimerizer was added to the axon chambers on DIV4–5 for 4 h. For experiment with 8-Br-cADPR, 8-Br-cADPR was added to axon chamber 1 h before paclitaxel or 50 nM B/B homodimerizer and continued to be present in axon together with paclitaxel or B/B homodimerizer.

For axotomy-induced axon degeneration, mouse DRG cultures were prepared as described previously (Sasaki et al., 2016). Briefly, DRG was dissected from embryonic days 13.5–14.5 CD1 mouse (Charles River Laboratories) and incubated with 0.05% Trypsin solution at 37°C for 20 min. Then, cell suspensions were triturated by gentle pipetting and washed with Neurobasal

culture medium (Gibco) containing 2% B27 (Invitrogen), 50 ng/ml NGF (Envigo Bioproducts; Cat. #B5017), 1  $\mu$ M uridine (Sigma-Aldrich), 1  $\mu$ M 5-fluoro-2'-deoxyuridine (Sigma-Aldrich), penicillin, and streptomycin. Cell suspensions were placed in the center of the well using a 24-well tissue culture plate (Corning) coated with poly-D-Lysine (0.1 mg/ml; Sigma-Aldrich) and laminin (3  $\mu$ g/ml; Invitrogen).

### LC-MS/MS analysis

Metabolites extraction was done following nucleotide extraction protocol provided by the McGill metabolic core facility. Briefly, both mass culture and Campenot culture were washed with ice-cold 150 mM ammonium formate buffer and harvested in ice-cold 50%/50% (vol/vol) methanol/LC-MS grade water, followed by three-solvent extraction (50% methanol/acetonitrile/dichloromethane/water = 380  $\mu$ l:220  $\mu$ l:600  $\mu$ l:300  $\mu$ l). The aqueous phase was then isolated and dried using vacuum centrifugation. For semiquantitative targeted metabolite analysis of nucleotides, samples were injected onto an Agilent 6470 Triple Quadrupole. Chromatography was achieved using a 1290 Infinity ultra-performance LC system (Agilent Technologies). Separation was performed on a Scherzo SM-C18 column 3  $\mu$ m, 3.0  $\times$  150 mm (Imtakt Corp) maintained at 10°C. The chromatographic gradient started at 100% mobile phase A (5 mM ammonium acetate in water) with a 5-min gradient to 100% B (200 mM ammonium acetate in 20% acetonitrile/80% water) at a flow rate of 0.4 ml/min. This was followed by a 5-min hold time at 100% mobile phase B and a subsequent reequilibration time (6 min) before next injection. Samples were individually resuspended in 30  $\mu$ l of cold water, and 5  $\mu$ l volume was injected immediately after sample preparation to help preserve unstable metabolites.

Multiple reaction monitoring (MRM) transitions were optimized on standards for each metabolite measured. MRM transitions and retention time windows are summarized in Table S4. An Agilent JetStream electrospray ionization source was used in positive ionization mode with gas temperature and flow set at 300°C and 5 liter/min, respectively; nebulizer pressure set at 45 psi; and capillary voltage set at 3,500 V. Relative concentrations were determined from external calibration curves prepared in water. Ion suppression artifacts were not corrected; thus, the presented metabolite levels are relative to the external calibration curves and should not be considered as absolute concentrations. Data were analyzed using MassHunter Quant (Agilent Technologies). The amount of each metabolite per sample was normalized to cell number. See Table S4 for a summary of MRM transitions and retention time windows

### Plasmids construction

For lentiviral constructs expression of Sarm1, RyR3, and CD38 shRNA, the following oligos were annealed and cloned into pLKO.1 between AgeI and EcoRI following instructions provided by Addgene (<https://www.addgene.org/protocols/plko/>): Sarm1: For: 5'-CCGGCAGGTAGATGGTGAATTTGCTTctcgagAAGCAAATCACCATCTACCTGTTTTTTT-3'; Rev: 5'-AATTCAAAAACAGGTAGATGGTGAATTTGCTTCTCGAGAAGCAAATCACCATCTACCTG-3'; RyR3: For: 5'-CCGGAAGCTCCTGACAAATCACTATCTCGA GATAGTGATTTGTCAGGAGCTTTTTTTT-3'; Rev: 5'-AATTCA

AAAAAAGCTCCTGACAAATCACTATCTCGAGATAGTGATTGTCAGGAGCTT-3'; CD38: For: 5'-CCGGGAGCATCCATCATGTAGACTTCTCGAGAA GTCTACATGATGGATGCTC-3'.

The shRNA sequence was selected using BLOCK-iT RNAi Designer provided by Thermo Fisher Scientific. Lentiviral constructs expressing shRNA targeting rat IP<sub>3</sub>R1 (TRCN0000321161) and TRPM2 (TRCN0000068488) were purchased from Sigma-Aldrich.

FCIV-hSarm1, a full-length isoform of the canonical 724-amino acid human SARM1, was introduced into lentivirus vector FCIV using the Takara HD InFusion Cloning Kit and complementary oligonucleotides. The expressed SARM1 protein contains optimized start codons K3, I4, H5 and is fused to 2 X Strep Tag at the N-terminus. The absence of mutations and other PCR errors was confirmed by sequencing (Genewiz). Generation of FCIV-FkbpF36V-Sarm1-TIR and FCIV-FkbpF36V-Myd88-TIR was previously described (Gerdt et al., 2015). Briefly, sTIR (AA560-724) was PCR amplified from human SARM1; human MYD-88 TIR (AA160-296) was synthesized as Gene Block fragments (IDT). Fkbp was PCR amplified from Cluc-Fkbp (Addgene; #31184) from the laboratory of David PiwnickaWorms. FkbpF36V variant was synthesized as a Gene Block (IDT). sTIR and mTIR were fused between FkbpF36V and Cerulean with flexible linkers and cloned into lentiviral FCIV vector.

### Lentivirus generation and transduction

Lentivirus was generated following protocols provided by Addgene (<https://www.addgene.org/protocols/plko/>). Briefly, transfer plasmid, packaging plasmid cytomegalovirus (pCMV)-dr8.91, and envelop plasmid pCMV-VSV-G were transfected into HEK293T cells using FUGENE6 or Lipofectamine2000 following manufacturer's instruction. The media containing virus were harvested 48 and 72 h after transfection and pooled and were then concentrated to ~1/12 of the original volume using Amicon Ultra-centrifugal filter. For lentivirus infection of DRG neurons in compartmented Campenot cultures, 25–50  $\mu$ l lentivirus was added to the middle chamber, which contains cell bodies, on DIV2. For microfluidic culture, 100  $\mu$ l lentivirus of TIR domains or 25  $\mu$ l lentivirus of shRNA was added to the cell body chamber on DIV1.

### Quantitative reverse transcription-PCR

RNA was extracted from DRG neurons using TRIzol (Invitrogen) according to manufacturer's instruction. Reverse transcription was performed using the SuperscriptIII first-strand synthesis (Thermo Fisher Scientific) according to the manufacturer's instruction, and quantitative real-time PCR was performed using Taqman Gene expression assays (Applied Biosystems) to analyze expression of SARM1 (Rn01750947\_m1), TRPM2 (Rn01429410\_m1), CD38 (Rn00565538\_m1), and RyR3 (Rn01486097\_m1). Data were normalized to GAPDH (Applied Biosystems) for each sample.

### Western blot

DRG neurons transduced with Sarm1, IP<sub>3</sub>R1, or control shRNA for 6–7 d were lysed with nonionic detergent. Lysates were



separated by 3–8% Tris-Acetate SDS-PAGE for IP<sub>3</sub>R1 and by 4–12% Bis-Tris SDS-Page for Sarm1 (Thermo Fisher Scientific) and probed with mouse anti-Sarm1 (1:10,000; [Chen et al., 2011](#)), rabbit anti-IP<sub>3</sub>R1 (1:1,000; Thermo Fisher Scientific; PA1-901), and rabbit anti-pan-actin (1:1,000; Cell Signaling; 8456S). Bands were visualized with secondary antibodies conjugated to HRP (1:10,000; Bio-Rad; 1721019, 1706516) and SuperSignal chemiluminescent substrates signal (Thermo Fisher Scientific). Blots were imaged using the AI600 Chemiluminescent Imager (GE Healthcare).

### Axonal degeneration assay

Neurons in Campenot cultures were fixed at room temperature with 4% PFA diluted 1:2 in media for 10 min, then undiluted 4% PFA for an additional 20 min. Cultures were permeabilized and blocked in 3% BSA and 0.1% Triton X-100 for 1 h at room temperature and incubated with mouse anti-Tuj1 (1:500; BioLegend; 801213) overnight at 4°C. Cultures were then washed twice with PBS and incubated with goat anti-mouse Alexa Fluor (1:400; Invitrogen; A11001) and DAPI for 1 h at room temperature. Campenot dividers were then removed, and samples were mounted with Fluoromount-G (Southern Biotech; 0100-01). Images of distal axon tips were obtained using NIS elements imaging software (Nikon) with a Nikon Eclipse E800 microscope with a 40× air objective and a Nikon Digital Sight DS U2 camera at room temperature; images were analyzed using ImageJ. Images were binarized, and axonal degeneration was quantified as degeneration index ratio of fragmented axons (particle size: 1–1,000) divided by total axon area in each image ([Pease-Raissi et al., 2017](#); [Sasaki et al., 2009](#)).

Neurons in microfluidic cultures were permeabilized and blocked in 3% BSA and 0.1% Triton X-100 for 1 h at room temperature and incubated with mouse anti-Tuj1 (1:500; BioLegend; 801213) overnight at 4°C. Cultures were then washed twice with PBS and incubated with donkey anti-mouse Alexa Fluor 488 (1:400; Invitrogen; A11001) and DAPI for 1 h at room temperature. Teflon dividers were then removed, and samples were mounted with Fluoromount-G (Southern Biotech; 0100-01). Images of 10–20 fields of axons for each sample were acquired using NIS elements imaging software (Nikon) with a Nikon Ti-E at room temperature (60× oil, 1.4 NA objective). The same XY positions were imaged for treatments and control for each experiment. Images were binarized, and axon area was measured using NIH ImageJ software. Data were then normalized to DMSO-treated control.

### Axotomy-induced axon degeneration assay

Mouse DRG neurons were placed in the center of the well using a 24-well tissue culture plate. On DIV7, 1 or 10 μM 8-Br-cADPR was preincubated 30 min before axon injury. Axons from DRG neurons were either transected using a microsurgical blade under a microscope or applied with 50 μM carbonyl cyanide m-chlorophenylhydrazone for axon degeneration assay. Bright-field images of distal axons (20 fields/well and 3 wells/conditions) were acquired at 0–24 h after axon injury using a high-content imager (Operetta; PerkinElmer) with a 20× water objective lens.

Axon degeneration was quantified using degeneration index calculated with ImageJ.

### Calcium imaging

E15 DRG neurons in microfluidic devices were transduced on DIV1 with 5–10 μl AAV9-axonal-GCaMP6s-P2A-mRuby3 ([Broussard et al., 2018](#); AAV9 was generated by Applied Biological Materials) alone or together with 25 μl lentivirus expressing shRNA-targeting tGFP, Sarm1, or CD38 for 24 h. Cultures were maintained in phenol red-free NeuroBasal medium supplemented with 2% B27, 1% Glutamax, 1% penicillin and streptomycin, 0.08% glucose, NGF/BDNF, and 0.5 μM AraC for 4–5 d before imaging. For neurons transduced with lentivirus-expressing shRNA, 1 μg/ml puromycin was added to the cell body on DIV3 for 2 d for selection and was removed before imaging. 8–10 fields of axon chamber for each sample were imaged using NIS-elements (Nikon) with a Nikon Ti-E at 37°C (60× oil, 1.4 NA objective) with 7.5% CO<sub>2</sub> before treatment as time zero. Then, 600 nM paclitaxel or 0.5% DMSO was added to axon compartments. Cultures were maintained in incubators at 37°C with 7.5% CO<sub>2</sub>. The same fields of axons for each sample were imaged manually at 12, 16, 20, 24, 36, 40, 44, and 48 h after treatment. For experiments with 8-Br-cADPR, 20 μM 8-Br-cADPR was added to axon chamber 1 h before paclitaxel and continued to be present in axon together with paclitaxel.

For FkbpF36V-sTIR-induced calcium flux, DIV1 DRG neurons were transduced with 5–10 μl AAV9-axonal-GCaMP6s-P2A-mRuby3 together with 100 μl lentivirus expressing FkbpF36V-sTIR or FkbpF36V-mTIR. Cultures were maintained in phenol red-free NeuroBasal medium supplemented with 2% B27, 1% Glutamax, 1% penicillin and streptomycin, 0.08% glucose, NGF/BDNF, and 0.5 μM AraC for 4–5 d before imaging. Expressions of FkbpF36V-sTIR or mTIR were verified based on Cerulean expression. Eight fields of axon chamber for each sample were imaged before treatment and every 1 h after addition of 50 nM B/B homodimerizer to the axon chamber. For experiments with 8-Br-cADPR, 10 μM 8-Br-cADPR was added to axon chamber 1 h before 50 nM B/B homodimerizer was added and continued to be present in the axon chamber.

Both GCaMP6s (FITC channel) and mRuby3 (TRITC channel) signals were acquired using NIS-elements (Nikon) at each time point using the Nikon Ti-E at 37°C (60× oil, 1.4 NA objective) with 7.5% CO<sub>2</sub>. Images were analyzed using NIH ImageJ software. For each field at each time point, background signal was subtracted for the individual fluorescent channel using ImageJ default “Subtract Background” function. Then, axon area was selected based on mRuby3 signal using the embedded “MinError” threshold setting. Then, GCaMP6s and mRuby3 fluorescence intensities within the defined axon area were measured. The axonal GCaMP6s for each field at each time point was normalized to the corresponding mRuby3 intensity. The change in fluorescence was measured per field of axons using the equation  $[(\text{GCaMP6s}/\text{mRuby})/(\text{GCaMP6s}/\text{mRuby})_0]$ , where  $(\text{GCaMP6s}/\text{mRuby})_0$  is the baseline at time 0 before treatment. Treatments and the corresponding controls were done in parallel for each independent experiment.

## Expression and purification of Sarm1 protein

Human SARM1 was transfected to a 150-mm-diameter cell culture dish with 50% confluence of HEK293T cells. 15  $\mu$ g of plasmid was mixed with 75  $\mu$ g of polyethylenimine (1 mg/ml, pH 7.0) and transfected to the cells. Cells were harvested 48 h after transfection and resuspended in 100 mM Tris-Cl, pH 8.0, and 150 mM NaCl with Protease Inhibitor Cocktail (Pierce) before being lysed with sonication on ice. After centrifugation at 18,000 $\times$ g for 10 min and three times to remove the cell debris, supernatant was mixed with PureCube HiCap Streptactin MagBeads (Cube Biotech) for 1 h. After washing three times with 25 mM Hepes, pH 7.5, and 150 mM NaCl, SARM1-laden beads were stored in the same buffer plus 1 mM tris(2-carboxyethyl) phosphine and were stored at  $-80^{\circ}\text{C}$ . Protein purity was assessed by 4–12% SDS-PAGE by Coomassie staining. Protein concentration was determined using ImageJ (NIH) against BSA standard with known concentrations running on the same SDS-PAGE.

## Sarm1 in vitro activity assay

Sarm1 in vitro activity was assessed as described previously with modification (Essuman et al., 2017). Briefly, human SARM1 (15 nM)-laden beads were mixed with various concentrations of 8-Br-cADPR in 50 mM Hepes, pH 7.5, 50  $\mu$ M NAD, and 25  $\mu$ M NMN at  $25^{\circ}\text{C}$ . Reaction was performed in a ThermoMixer. At various time points, the reaction was stopped by taking 50  $\mu$ l from the reaction mixture and mixing with 50  $\mu$ l 0.5M perchloric acid ( $\text{HClO}_4$ ) before placing on ice for 10 min. After centrifugation at 18,000 $\times$ g for 10 min, supernatant was mixed with 6  $\mu$ l 3M  $\text{K}_2\text{CO}_3$  for neutralization. Samples were placed on ice for another 10 min and centrifuged one more time. 45  $\mu$ l of supernatant containing extracted metabolites was mixed with 5  $\mu$ l 0.5 M potassium Pphosphate buffer and quantified by HPLC (Nexera X2) with Kinetex (100  $\times$  3 mm, 2.6  $\mu$ m; Phenomenex) column. ADPR and Nam production rates were calculated from samples taken at various time points at each 8-Br-cADPR concentration.

## Paclitaxel treatment in vivo and behavioral testing

2-mo-old C57BL6/J mice (18–25 g) of both sexes were injected i.p. with 20 mg/kg paclitaxel (Bristol-Myers Squibb) every other day (days 1, 3, 5, and 7, for a total of four injections), while 2 mg/kg 8-Br-cADPR was injected after every two paclitaxel injections (days 4 and 8, for a total of two injections). Paclitaxel was prepared in one part vehicle (1:1 vol/vol Cremophor EL [EMD Millipore] and 200-proof ethanol) and two parts sterile saline (UPS) and injected at 10  $\mu$ l/g. Control mice were injected with one part vehicle and two parts saline. 8-Br-cADPR (Sigma-Aldrich) was prepared in sterile saline and injected at 10  $\mu$ l/g, and control mice were injected with saline. Mice were habituated for 2 d, and baseline behavioral performance was assessed over the next 2 d and averaged. The first paclitaxel injection (day 1) was given 3 d later, and mice were behaviorally tested 9 d after the final injection (day 17). Noxious mechanosensation threshold was assayed as described previously (Pease-Raissi et al., 2017) using Von Frey filaments (0.008–1.4 g). Withdrawal threshold was determined to be the applied force at which the animal withdrew the stimulated paw on at least 2 of 10 applications.

## Tumor-bearing mice

E0771 mouse breast tumor cells (American Type Culture Collection) were injected ( $2 \times 10^5$  cells/injection) orthotopically into the thoracic fat pads of 2-mo-old C57BL/6J female mice (The Jackson Laboratory) in 40% Matrigel. 7 d after tumor cells injection, paclitaxel or vehicle was injected i.p. every other day for 16 d (days 1, 3, 5, 7, 9, 11, 13, and 15, for a total of eight injections; 4 mg/kg for the first two injections and 20 mg/kg for the remaining six injections). 8-Br-cADPR or saline was injected i.p. after every two injections of paclitaxel (days 4, 8, 12, and 16, for a total of four injections; 2 mg/kg each injection). Tumor size and animal weight were measured before the first paclitaxel injection and every 3–4 d after. Tumor size was assessed by measuring the long and short axes, and volume was calculated by use of the modified ellipsoid formula ( $\text{long} \times \text{short}^2 \times 0.5$ ). The size of each tumor was normalized to the tumor size acquired on the day before the first injection of paclitaxel.

## Epidermal footpad innervation

Mice hindpaw footpads were prepared as described (Pease-Raissi et al., 2017). Briefly, mice were euthanized with isoflurane, and footpad tissue was removed and divided into thick (dermal papillae-containing footpad region) and thin (non-dermal papillae-containing plantar metatarsal region) skin. Footpads were fixed in Zamboni's fixative overnight at  $4^{\circ}\text{C}$ , cryopreserved in 30% sucrose in PBS for 2 d at  $4^{\circ}\text{C}$ , frozen, and sectioned into 30- $\mu$ m floating sections. Sections were permeabilized and blocked with 0.1% Triton X-100 in PBS supplemented with 10% normal goat serum for 1 h at room temperature and incubated with mouse anti-Tuj1 (1:300; BioLegend; 801213) overnight at  $4^{\circ}\text{C}$ . Sections were then incubated with goat anti-mouse Alexa Fluor 488 (1:200; Invitrogen; A11001) and DAPI (1:1,000; Invitrogen) for 2 h at room temperature and mounted on gelatin-coated slides. IENF images were acquired using NIS-elements (Nikon) on a Nikon Ni-E C2 confocal with a 40 $\times$ , 1.3 NA oil objective as 30–31- $\mu$ m z-stacks at room temperature and converted to maximum-intensity projection image for quantification. IENF density was counted and calculated as the number of Tuj1-positive fibers extending into the epidermis per 100- $\mu$ m epidermal length. Epidermal length was determined using the embedded “measure length” function of NIS-elements (Nikon).

## Quantification and statistical analysis

Data are expressed as mean  $\pm$  SEM. For grouped data multiple comparisons, data were analyzed by two-way ANOVA with Tukey's multiple comparisons test. For columned data multiple comparisons, data were analyzed by one-way ANOVA with Tukey's multiple comparisons test. For calcium imaging, data were analyzed by two-way ANOVA, and data at each time point were compared using Tukey's multiple comparisons test. Significance was placed at \*,  $P < 0.05$ ; \*\*,  $P < 0.01$ ; \*\*\*,  $P < 0.001$ ; \*\*\*\*,  $P < 0.0001$ . Statistical analysis was done using GraphPad Prism. Data distribution was assumed to be normal, but this was not formally tested.

## Online supplemental material

Fig. S1 presents data related to Fig. 1: verification of knockdown by shRNAs targeted to Sarm1 and CD38; CD38 depletion alone does not lead to axon degeneration in DRG neurons, and

paclitaxel does not affect ADPR levels in vitro. Fig. S2 presents data related to Fig. 2: paclitaxel decreases overall axon area in a dose-dependent fashion in DRGs, and axonal degeneration follows calcium elevation in paclitaxel-treated DRGs. Fig. S3 presents data related to Fig. 3 and Fig. 4: schematic illustration of chemical-induced sTIR dimerization and Sarm1 depletion provided stronger neuroprotection against paclitaxel than 8-Br-cADPR in vitro. Fig. S4 presents data related to Fig. 5: verification of knockdown by shRNAs targeted to RyR3, IP<sub>3</sub>R1, and TRPM2, mTIR dimerization does not cause axon degeneration, and 8-Br-ADPR protects against paclitaxel-induced axon degeneration in vitro. Fig. S5 presents data related to Fig. 6 and Fig. 7: 8-Br-cADPR protects against paclitaxel-induced peripheral neuropathy in vivo without causing weight change of animals.

Table S1, Table S2, Table S3, Table S4, and Table S5 present statistics results of Fig. 1, D–F, summary of MRM transitions and retention time windows of LC-MS, and key resources and reagents.

### Data availability

Further information and requests for resources and reagents should be directed to and will be fulfilled by the lead contact, Rosalind Segal (rosalind\_segal@dfci.harvard.edu).

### Acknowledgments

We thank Timothy Walseth (University of Minnesota) for comments and discussion on cADPR functions. We thank Nika Danial, Accalia Fu, and M. Carmen Fernandez-Aguera for discussion on metabolic studies. We thank the Segal laboratory and Stiles laboratory for helpful comments on the manuscript.

This work was supported by the Edward R. and Anne G. Lefler Center Postdoctoral Fellowship to Y. Li, Friends of Dana-Farber Cancer Institute grant to J.S. Bergholz, Breast Cancer Research Foundation grant to J.J. Zhao, and the National Institutes of Health grants R35 CA210057 to J.J. Zhao, R01 CA205255 to R.A. Segal, and R01 CA219866 and R01 NS087632 to A. DiAntonio and J. Milbrandt.

The authors declare no competing financial interests. J.S. Bergholz is a scientific consultant for Geode Therapeutics Inc. T. Jiang is a scientific consultant for Crimson Biotech Inc. J.J. Zhao is a cofounder and board director of Crimson Biotech Inc. and Geode Therapeutics Inc. A. DiAntonio and J. Milbrandt are cofounders, scientific advisory board members, and shareholders of Disarm Therapeutics.

Author contributions: Y. Li, M.F. Pazyra-Murphy, D. Avizonis, J.J. Zhao, A. DiAntonio, J. Milbrandt, and R.A. Segal designed research. Y. Li, M.F. Pazyra-Murphy, S. Tang, M.D.S.T. Russo, D. Avizonis, J.S. Bergholz, T. Jiang, J. Zhu, and K.W. Ko performed research. Y. Li, M.F. Pazyra-Murphy, S. Tang, M.D.S.T. Russo, D. Avizonis, J. Zhu, and K.W. Ko analyzed data. C.-Y. Chen, and Y.P. Hsueh provided critical reagent. Y. Li and R.A. Segal wrote the paper with input from M.F. Pazyra-Murphy, A. DiAntonio, J. Milbrandt, J.S. Bergholz, J.J. Zhao, M.D.S.T. Russo, and D. Avizonis.

Submitted: 14 June 2021

Revised: 17 October 2021

Accepted: 7 December 2021

### References

- Adalbert, R., G. Morreale, M. Paizs, L. Conforti, S.A. Walker, H.L. Roderick, M.D. Bootman, L. Siklós, and M.P. Coleman. 2012. Intra-axonal calcium changes after axotomy in wild-type and slow Wallerian degeneration axons. *Neuroscience*. 225:44–54. <https://doi.org/10.1016/j.neuroscience.2012.08.056>
- Aksoy, P., T.A. White, M. Thompson, and E.N. Chini. 2006. Regulation of intracellular levels of NAD: a novel role for CD38. *Biochem. Biophys. Res. Commun.* 345:1386–1392. <https://doi.org/10.1016/j.bbrc.2006.05.042>
- Banerjee, S., T.F. Walseth, K. Borgmann, L. Wu, K.R. Bidasee, M.S. Kannan, and A. Ghorpade. 2008. CD38/cyclic ADP-ribose regulates astrocyte calcium signaling: implications for neuroinflammation and HIV-1-associated dementia. *J. Neuroimmune Pharmacol.* 3:154–164.
- Benbow, J.H., T. Mann, C. Keeler, C. Fan, M.E. Hodsdon, E. Lolis, B. DeGray, and B.E. Ehrlich. 2012. Inhibition of paclitaxel-induced decreases in calcium signaling. *J. Biol. Chem.* 287:37907–37916. <https://doi.org/10.1074/jbc.M112.385070>
- Berbusse, G.W., L.C. Woods, B.P. Vohra, and K. Naylor. 2016. Mitochondrial Dynamics Decrease Prior to Axon Degeneration Induced by Vincristine and are Partially Rescued by Overexpressed cytnmna1. *Front. Cell. Neurosci.* 10:179. <https://doi.org/10.3389/fncel.2016.00179>
- Bobylev, I., A.R. Joshi, M. Barham, C. Ritter, W.F. Neiss, A. Höke, and H.C. Lehmann. 2015. Paclitaxel inhibits mRNA transport in axons. *Neurobiol. Dis.* 82:321–331. <https://doi.org/10.1016/j.nbd.2015.07.006>
- Boehmerle, W., K. Zhang, M. Sivula, F.M. Heidrich, Y. Lee, S.E. Jordt, and B.E. Ehrlich. 2007. Chronic exposure to paclitaxel diminishes phosphoinositide signaling by calpain-mediated neuronal calcium sensor-1 degradation. *Proc. Natl. Acad. Sci. USA*. 104:11103–11108. <https://doi.org/10.1073/pnas.0701546104>
- Bourgeois-Daigneault, M.C., L.E. St-Germain, D.G. Roy, A. Pelin, A.S. Aitken, R. Arulanandam, T. Falls, V. Garcia, J.S. Diallo, and J.C. Bell. 2016. Combination of Paclitaxel and MGI oncolytic virus as a successful strategy for breast cancer treatment. *Breast Cancer Res.* 18:83. <https://doi.org/10.1186/s13058-016-0744-y>
- Broussard, G.J., Y. Liang, M. Fridman, E.K. Unger, G. Meng, X. Xiao, N. Ji, L. Petreanu, and L. Tian. 2018. In vivo measurement of afferent activity with axon-specific calcium imaging. *Nat. Neurosci.* 21:1272–1280. <https://doi.org/10.1038/s41593-018-0211-4>
- Cetinkaya-Figgin, A., X. Luan, N. Reed, Y.E. Jeong, B.C. Oh, and A. Hoke. 2020. Cisplatin induced neurotoxicity is mediated by Sarm1 and calpain activation. *Sci. Rep.* 10:21889. <https://doi.org/10.1038/s41598-020-78896-w>
- Chen, C.Y., C.W. Lin, C.Y. Chang, S.T. Jiang, and Y.P. Hsueh. 2011. Sarm1, a negative regulator of innate immunity, interacts with syndecan-2 and regulates neuronal morphology. *J. Cell Biol.* 193:769–784. <https://doi.org/10.1083/jcb.201008050>
- Chini, E.N. 2009. CD38 as a regulator of cellular NAD: a novel potential pharmacological target for metabolic conditions. *Curr. Pharm. Des.* 15: 57–63. <https://doi.org/10.2174/138161209787185788>
- Clapper, D.L., T.F. Walseth, P.J. Dargie, and H.C. Lee. 1987. Pyridine nucleotide metabolites stimulate calcium release from sea urchin egg microsomes desensitized to inositol trisphosphate. *J. Biol. Chem.* 262: 9561–9568. [https://doi.org/10.1016/S0021-9258\(18\)47970-7](https://doi.org/10.1016/S0021-9258(18)47970-7)
- Currie, K.P., K. Swann, A. Galione, and R.H. Scott. 1992. Activation of Ca(2+)-dependent currents in cultured rat dorsal root ganglion neurones by a sperm factor and cyclic ADP-ribose. *Mol. Biol. Cell.* 3:1415–1425. <https://doi.org/10.1091/mbc.3.12.1415>
- Dargie, P.J., M.C. Agre, and H.C. Lee. 1990. Comparison of Ca2+ mobilizing activities of cyclic ADP-ribose and inositol trisphosphate. *Cell Regul.* 1: 279–290. <https://doi.org/10.1091/mbc.1.3.279>
- Dorsey, S.G., I.R. Kleckner, D. Barton, K. Mustian, A. O'Mara, D. St Germain, G. Cavaletti, S.C. Danhauer, D.L. Hershman, A.G. Hohmann, et al. 2019. The National Cancer Institute Clinical Trials Planning Meeting for Prevention and Treatment of Chemotherapy-Induced Peripheral Neuropathy. *J. Natl. Cancer Inst.* 111:531–537. <https://doi.org/10.1093/jnci/djz011>
- Essuman, K., D.W. Summers, Y. Sasaki, X. Mao, A. DiAntonio, and J. Milbrandt. 2017. The SARM1 Toll/Interleukin-1 Receptor Domain Possesses Intrinsic NAD<sup>+</sup> Cleavage Activity that Promotes Pathological Axonal Degeneration. *Neuron*. 93:1334–1343.e5. <https://doi.org/10.1016/j.neuron.2017.02.022>
- Fenstermacher, S.J., M.F. Pazyra-Murphy, and R.A. Segal. 2015. Campenot cultures and microfluidics provide complementary platforms for spatial study of dorsal root ganglia neurons. In *Microfluidic and Compartmentalized Platforms for Neurobiological Research*. E. Biffi, editor.



- Springer New York, New York. 105–124. [https://doi.org/10.1007/978-1-4939-2510-0\\_6](https://doi.org/10.1007/978-1-4939-2510-0_6)
- Figley, M.D., W. Gu, J.D. Nanson, Y. Shi, Y. Sasaki, K. Cunnea, A.K. Malde, X. Jia, Z. Luo, F.K. Saikot, et al. 2021. SARM1 is a metabolic sensor activated by an increased NMN/NAD<sup>+</sup> ratio to trigger axon degeneration. *Neuron*. 109:1118–1136.e11. <https://doi.org/10.1016/j.neuron.2021.02.009>
- Fukuda, Y., Y. Li, and R.A. Segal. 2017. A Mechanistic Understanding of Axon Degeneration in Chemotherapy-Induced Peripheral Neuropathy. *Front. Neurosci.* 11:481. <https://doi.org/10.3389/fnins.2017.00481>
- Galione, A., and A. White. 1994. Ca<sup>2+</sup> release induced by cyclic ADP-ribose. *Trends Cell Biol.* 4:431–436. [https://doi.org/10.1016/0962-8924\(94\)90104-X](https://doi.org/10.1016/0962-8924(94)90104-X)
- Galione, A., H.C. Lee, and W.B. Busa. 1991. Ca(2+)-induced Ca2+ release in sea urchin egg homogenates: modulation by cyclic ADP-ribose. *Science*. 253:1143–1146. <https://doi.org/10.1126/science.1909457>
- Geisler, S., R.A. Doan, A. Strickland, X. Huang, J. Milbrandt, and A. DiAntonio. 2016. Prevention of vincristine-induced peripheral neuropathy by genetic deletion of SARM1 in mice. *Brain*. 139:3092–3108. <https://doi.org/10.1093/brain/aww251>
- Geisler, S., R.A. Doan, G.C. Cheng, A. Cetinkaya-Fisgin, S.X. Huang, A. Höke, J. Milbrandt, and A. DiAntonio. 2019a. Vincristine and bortezomib use distinct upstream mechanisms to activate a common SARM1-dependent axon degeneration program. *JCI Insight*. 4:e129920. <https://doi.org/10.1172/jci.insight.129920>
- Geisler, S., S.X. Huang, A. Strickland, R.A. Doan, D.W. Summers, X. Mao, J. Park, A. DiAntonio, and J. Milbrandt. 2019b. Gene therapy targeting SARM1 blocks pathological axon degeneration in mice. *J. Exp. Med.* 216:294–303. <https://doi.org/10.1084/jem.20181040>
- Gerdt, J., D.W. Summers, Y. Sasaki, A. DiAntonio, and J. Milbrandt. 2013. Sarm1-mediated axon degeneration requires both SAM and TIR interactions. *J. Neurosci.* 33:13569–13580. <https://doi.org/10.1523/JNEUROSCI.1197-13.2013>
- Gerdt, J., E.J. Brace, Y. Sasaki, A. DiAntonio, and J. Milbrandt. 2015. SARM1 activation triggers axon degeneration locally via NAD<sup>+</sup> destruction. *Science*. 348:453–457. <https://doi.org/10.1126/science.1258366>
- Gilley, J., and M.P. Coleman. 2010. Endogenous Nmnat2 is an essential survival factor for maintenance of healthy axons. *PLoS Biol.* 8:e1000300. <https://doi.org/10.1371/journal.pbio.1000300>
- Gilley, J., G. Orsomando, I. Nascimento-Ferreira, and M.P. Coleman. 2015. Absence of SARM1 rescues development and survival of NMNAT2-deficient axons. *Cell Rep.* 10:1974–1981. <https://doi.org/10.1016/j.celrep.2015.02.060>
- Gornstein, E.L., and T.L. Schwarz. 2017. Neurotoxic mechanisms of paclitaxel are local to the distal axon and independent of transport defects. *Exp. Neurol.* 288:153–166. <https://doi.org/10.1016/j.expneurol.2016.11.015>
- Guse, A.H. 1999. Cyclic ADP-ribose: a novel Ca<sup>2+</sup>-mobilising second messenger. *Cell. Signal.* 11:309–316. [https://doi.org/10.1016/S0898-6568\(99\)00004-2](https://doi.org/10.1016/S0898-6568(99)00004-2)
- Guse, A.H., C.P. da Silva, I. Berg, A.L. Skapenko, K. Weber, P. Heyer, M. Hohenegger, G.A. Ashamu, H. Schulze-Koops, B.V. Potter, and G.W. Mayr. 1999. Regulation of calcium signalling in T lymphocytes by the second messenger cyclic ADP-ribose. *Nature*. 398:70–73. <https://doi.org/10.1038/18024>
- Han, Y., and M.T. Smith. 2013. Pathobiology of cancer chemotherapy-induced peripheral neuropathy (CIPN). *Front. Pharmacol.* 4:156. <https://doi.org/10.3389/fphar.2013.00156>
- Higashida, H., M. Hashii, S. Yokoyama, N. Hoshi, K. Asai, and T. Kato. 2001. Cyclic ADP-ribose as a potential second messenger for neuronal Ca<sup>2+</sup> signaling. *J. Neurochem.* 76:321–331. <https://doi.org/10.1046/j.1471-4159.2001.00082.x>
- Huang, Y., P.A. Winkler, W. Sun, W. Lü, and J. Du. 2018. Architecture of the TRPM2 channel and its activation mechanism by ADP-ribose and calcium. *Nature*. 562:145–149. <https://doi.org/10.1038/s41586-018-0558-4>
- Hughes, R.O., T. Bosanac, X. Mao, T.M. Engber, A. DiAntonio, J. Milbrandt, R. Devraj, and R. Krauss. 2021. Small Molecule SARM1 Inhibitors Recapitulate the SARM1<sup>-/-</sup> Phenotype and Allow Recovery of a Metastable Pool of Axons Fated to Degenerate. *Cell Rep.* 34:108588. <https://doi.org/10.1016/j.celrep.2020.108588>
- Ko, K.W., J. Milbrandt, and A. DiAntonio. 2020. SARM1 acts downstream of neuroinflammatory and necroptotic signaling to induce axon degeneration. *J. Cell Biol.* 219:e201912047. <https://doi.org/10.1083/jcb.201912047>
- Kolisek, M., A. Beck, A. Fleig, and R. Penner. 2005. Cyclic ADP-ribose and hydrogen peroxide synergize with ADP-ribose in the activation of TRPM2 channels. *Mol. Cell.* 18:61–69. <https://doi.org/10.1016/j.molcel.2005.02.033>
- Lee, H.C. 1993. Potentiation of calcium- and caffeine-induced calcium release by cyclic ADP-ribose. *J. Biol. Chem.* 268:293–299. [https://doi.org/10.1016/S0021-9258\(18\)54148-X](https://doi.org/10.1016/S0021-9258(18)54148-X)
- Lee, H.C., T.F. Walseth, G.T. Bratt, R.N. Hayes, and D.L. Clapper. 1989. Structural determination of a cyclic metabolite of NAD<sup>+</sup> with intracellular Ca<sup>2+</sup>-mobilizing activity. *J. Biol. Chem.* 264:1608–1615. [https://doi.org/10.1016/S0021-9258\(18\)94230-4](https://doi.org/10.1016/S0021-9258(18)94230-4)
- Lokuta, A.J., H. Komai, T.S. McDowell, and H.H. Valdivia. 2002. Functional properties of ryanodine receptors from rat dorsal root ganglia. *FEBS Lett.* 511:90–96. [https://doi.org/10.1016/S0014-5793\(01\)03312-9](https://doi.org/10.1016/S0014-5793(01)03312-9)
- Loreto, A., M. Di Stefano, M. Gering, and L. Conforti. 2015. Wallerian Degeneration Is Executed by an NMN-SARM1-Dependent Late Ca(2+) Influx but Only Modestly Influenced by Mitochondria. *Cell Rep.* 13:2539–2552. <https://doi.org/10.1016/j.celrep.2015.11.032>
- Mészáros, L.G., J. Bak, and A. Chu. 1993. Cyclic ADP-ribose as an endogenous regulator of the non-skeletal type ryanodine receptor Ca<sup>2+</sup> channel. *Nature*. 364:76–79. <https://doi.org/10.1038/364076a0>
- Moreau, C., G.A. Ashamu, V.C. Bailey, A. Galione, A.H. Guse, and B.V. Potter. 2011. Synthesis of cyclic adenosine 5'-diphosphate ribose analogues: a C2'endo/syn "southern" ribose conformation underlies activity at the sea urchin cADPR receptor. *Org. Biomol. Chem.* 9:278–290. <https://doi.org/10.1039/C0OB00396D>
- Mukherjee, P., T.A. Woods, R.A. Moore, and K.E. Peterson. 2013. Activation of the innate signaling molecule MAVS by bunyavirus infection upregulates the adaptor protein SARM1, leading to neuronal death. *Immunity*. 38:705–716. <https://doi.org/10.1016/j.immuni.2013.02.013>
- Osterloh, J.M., J. Yang, T.M. Rooney, A.N. Fox, R. Adalbert, E.H. Powell, A.E. Sheehan, M.A. Avery, R. Hackett, M.A. Logan, et al. 2012. dSarm/Sarm1 is required for activation of an injury-induced axon death pathway. *Science*. 337:481–484. <https://doi.org/10.1126/science.1223899>
- Partida-Sánchez, S., D.A. Cockayne, S. Monard, E.L. Jacobson, N. Oppenheimer, B. Garvy, K. Kusser, S. Goodrich, M. Howard, A. Harmsen, et al. 2001. Cyclic ADP-ribose production by CD38 regulates intracellular calcium release, extracellular calcium influx and chemotaxis in neutrophils and is required for bacterial clearance in vivo. *Nat. Med.* 7:1209–1216. <https://doi.org/10.1038/nm1101-1209>
- Partida-Sánchez, S., A. Gasser, R. Fliegert, C.C. Siebrands, W. Dammermann, G. Shi, B.J. Mousseau, A. Sumoza-Toledo, H. Bhagat, T.F. Walseth, et al. 2007. Chemotaxis of mouse bone marrow neutrophils and dendritic cells is controlled by adp-ribose, the major product generated by the CD38 enzyme reaction. *J. Immunol.* 179:7827–7839. <https://doi.org/10.4049/jimmunol.179.11.7827>
- Pease-Raissi, S.E., M.F. Pazyra-Murphy, Y. Li, F. Wachter, Y. Fukuda, S.J. Fenstermacher, L.A. Barclay, G.H. Bird, L.D. Walensky, and R.A. Segal. 2017. Paclitaxel Reduces Axonal Bclw to Initiate IP<sub>3</sub>R1-Dependent Axon Degeneration. *Neuron*. 96:373–386.e6. <https://doi.org/10.1016/j.neuron.2017.09.034>
- Rakovic, S., A. Galione, G.A. Ashamu, B.V. Potter, and D.A. Terrar. 1996. A specific cyclic ADP-ribose antagonist inhibits cardiac excitation-contraction coupling. *Curr. Biol.* 6:989–996. [https://doi.org/10.1016/S0960-9822\(02\)00643-7](https://doi.org/10.1016/S0960-9822(02)00643-7)
- Sasaki, Y., B.P. Vohra, F.E. Lund, and J. Milbrandt. 2009. Nicotinamide mononucleotide adenyllyl transferase-mediated axonal protection requires enzymatic activity but not increased levels of neuronal nicotinamide adenine dinucleotide. *J. Neurosci.* 29:5525–5535. <https://doi.org/10.1523/JNEUROSCI.5469-08.2009>
- Sasaki, Y., T. Nakagawa, X. Mao, A. DiAntonio, and J. Milbrandt. 2016. NMNAT1 inhibits axon degeneration via blockade of SARM1-mediated NAD<sup>+</sup> depletion. *eLife*. 5:e19749. <https://doi.org/10.7554/eLife.19749>
- Sasaki, Y., T.M. Engber, R.O. Hughes, M.D. Figley, T. Wu, T. Bosanac, R. Devraj, J. Milbrandt, R. Krauss, and A. DiAntonio. 2020. cADPR is a gene dosage-sensitive biomarker of SARM1 activity in healthy, compromised, and degenerating axons. *Exp. Neurol.* 329:113252. <https://doi.org/10.1016/j.expneurol.2020.113252>
- Schneider, B.P., D.L. Hershman, and C. Loprinzi. 2015. Symptoms: Chemotherapy-Induced Peripheral Neuropathy. *Adv. Exp. Med. Biol.* 862:77–87. [https://doi.org/10.1007/978-3-319-16366-6\\_6](https://doi.org/10.1007/978-3-319-16366-6_6)
- Seretny, M., G.L. Currie, E.S. Sena, S. Ramnarine, R. Grant, M.R. MacLeod, L.A. Colvin, and M. Fallon. 2014. Incidence, prevalence, and predictors of chemotherapy-induced peripheral neuropathy: A systematic review and meta-analysis. *Pain*. 155:2461–2470. <https://doi.org/10.1016/j.pain.2014.09.020>
- Shin, G.J.-e., M.E. Pero, L.A. Hammond, A. Burgos, A. Kumar, S.E. Galindo, T. Lucas, F. Bartolini, and W.B. Grueber. 2021. Integrins protect sensory neurons in models of paclitaxel-induced peripheral sensory

- neuropathy. *Proc. Natl. Acad. Sci. USA*. 118:e2006050118. <https://doi.org/10.1073/pnas.2006050118>
- Sonnleitner, A., A. Conti, F. Bertocchini, H. Schindler, and V. Sorrentino. 1998. Functional properties of the ryanodine receptor type 3 (RyR3) Ca<sup>2+</sup> release channel. *EMBO J.* 17:2790–2798. <https://doi.org/10.1093/emboj/17.10.2790>
- Stewart, T.A., K.T. Yapa, and G.R. Monteith. 2015. Altered calcium signaling in cancer cells. *Biochim. Biophys. Acta*. 1848(10 Pt B):2502–2511. <https://doi.org/10.1016/j.bbame.2014.08.016>
- Summers, D.W., D.A. Gibson, A. DiAntonio, and J. Milbrandt. 2016. SARM1-specific motifs in the TIR domain enable NAD<sup>+</sup> loss and regulate injury-induced SARM1 activation. *Proc. Natl. Acad. Sci. USA*. 113:E6271–E6280. <https://doi.org/10.1073/pnas.1601506113>
- Tian, W., T. Czopka, and H. López-Schier. 2020. Systemic loss of Sarm1 protects Schwann cells from chemotoxicity by delaying axon degeneration. *Commun. Biol.* 3:49. <https://doi.org/10.1038/s42003-020-0776-9>
- Turkiew, E., D. Falconer, N. Reed, and A. Höke. 2017. Deletion of Sarm1 gene is neuroprotective in two models of peripheral neuropathy. *J. Peripher. Nerv. Syst.* 22:162–171. <https://doi.org/10.1111/jns.12219>
- Vargas, M.E., Y. Yamagishi, M. Tessier-Lavigne, and A. Sagasti. 2015. Live Imaging of Calcium Dynamics during Axon Degeneration Reveals Two Functionally Distinct Phases of Calcium Influx. *J. Neurosci.* 35:15026–15038. <https://doi.org/10.1523/JNEUROSCI.2484-15.2015>
- Villegas, R., N.W. Martinez, J. Lillo, P. Pihan, D. Hernandez, J.L. Twiss, and F.A. Court. 2014. Calcium release from intra-axonal endoplasmic reticulum leads to axon degeneration through mitochondrial dysfunction. *J. Neurosci.* 34:7179–7189. <https://doi.org/10.1523/JNEUROSCI.4784-13.2014>
- Walseth, T.F., and H.C. Lee. 1993. Synthesis and characterization of antagonists of cyclic-ADP-ribose-induced Ca<sup>2+</sup> release. *Biochim. Biophys. Acta*. 1178:235–242. [https://doi.org/10.1016/0167-4889\(93\)90199-Y](https://doi.org/10.1016/0167-4889(93)90199-Y)
- Wan, L., K. Essuman, R.G. Anderson, Y. Sasaki, F. Monteiro, E.H. Chung, E. Osborne Nishimura, A. DiAntonio, J. Milbrandt, J.L. Dangel, and M.T. Nishimura. 2019. TIR domains of plant immune receptors are NAD<sup>+</sup>-cleaving enzymes that promote cell death. *Science*. 365:799–803. <https://doi.org/10.1126/science.aax1771>
- Wang, M.S., A.A. Davis, D.G. Culver, Q. Wang, J.C. Powers, and J.D. Glass. 2004. Calpain inhibition protects against Taxol-induced sensory neuropathy. *Brain*. 127:671–679. <https://doi.org/10.1093/brain/awh078>
- Wang, J.T., Z.A. Medress, and B.A. Barres. 2012. Axon degeneration: molecular mechanisms of a self-destruction pathway. *J. Cell Biol.* 196:7–18. <https://doi.org/10.1083/jcb.201108111>
- Yang, I.H., R. Siddique, S. Hosmane, N. Thakor, and A. Höke. 2009. Compartmentalized microfluidic culture platform to study mechanism of paclitaxel-induced axonal degeneration. *Exp. Neurol.* 218:124–128. <https://doi.org/10.1016/j.expneurol.2009.04.017>
- Yang, Z., Z. Yue, X. Ma, and Z. Xu. 2020. Calcium Homeostasis: A Potential Vicious Cycle of Bone Metastasis in Breast Cancers. *Front. Oncol.* 10:293. <https://doi.org/10.3389/fonc.2020.00293>
- Yu, P., Z. Liu, X. Yu, P. Ye, H. Liu, X. Xue, L. Yang, Z. Li, Y. Wu, C. Fang, et al. 2019. Direct Gating of the TRPM2 Channel by cADPR via Specific Interactions with the ADPR Binding Pocket. *Cell Rep.* 27:3684–3695.e4. <https://doi.org/10.1016/j.celrep.2019.05.067>

## Supplemental material



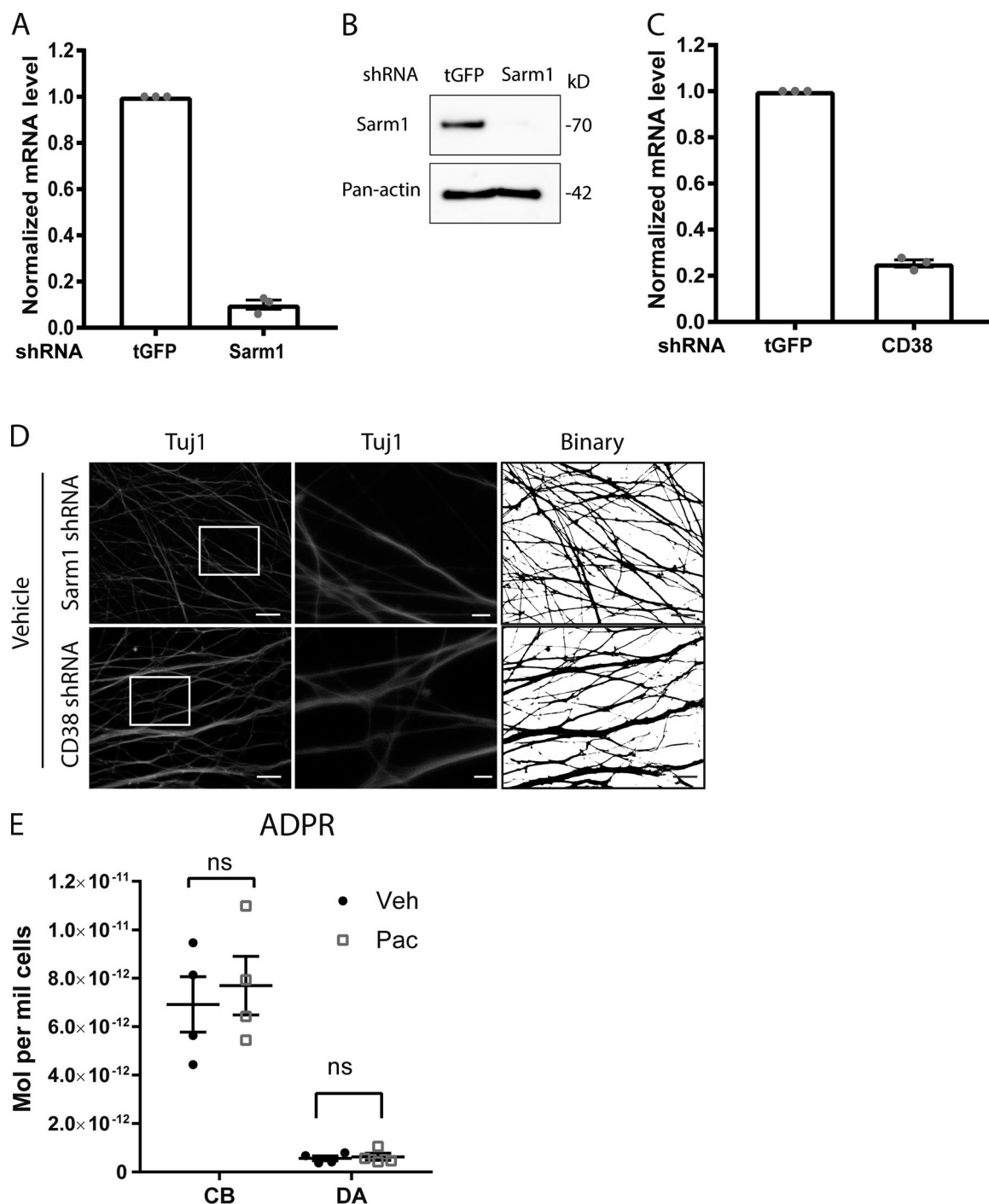


Figure S1. **Verification of knockdown by shRNAs targeted to Sarm1 and CD38, CD38 depletion alone does not lead to axon degeneration in DRG neurons, and paclitaxel does not affect ADPR levels in vitro.** (A) Normalized mRNA level of DRG neurons showing knockdown efficiency of Sarm1 shRNA compared with tGFP-control shRNA. Data represent mean  $\pm$  SEM; individual data points are shown. N represents three independent experiments. (B) Western blot probed against Sarm1 and pan-actin showing knockdown efficiency of Sarm1 shRNA in DRG neurons. (C) Normalized mRNA level of DRG neurons showing knockdown efficiency of CD38 shRNA compared with tGFP-control shRNA. Data represent mean  $\pm$  SEM; individual data points are shown. N represents three independent experiments. (D) Tuj1 immunostaining and corresponding binarized images of DRG axons transduced with Sarm1 shRNA or CD38 shRNA treated with DMSO (Veh). Scale bar: 20  $\mu$ m (left and right panels), 50  $\mu$ m (middle insets). (E) ADPR level in cell bodies (CB) and distal axons (DA) of DRGs after 24 h of 30 nM paclitaxel (Pac) or DMSO (Veh) added to axons. Data represent mean  $\pm$  SEM; individual data points are shown. N represents four independent experiments.

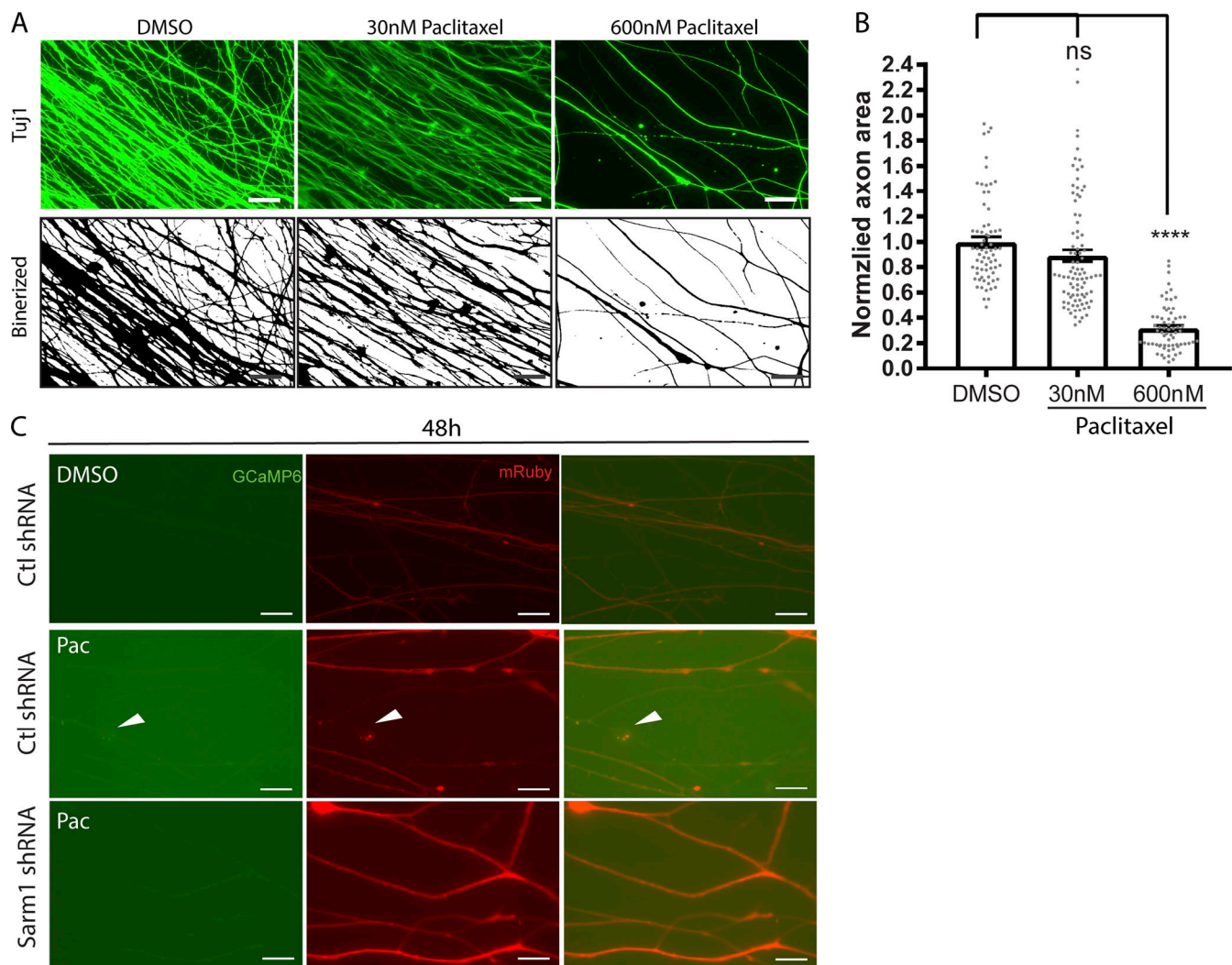


Figure S2. **Paclitaxel decreases overall axon area in a dose-dependent fashion in DRGs, and axonal degeneration follows calcium elevation in paclitaxel-treated DRGs.** (A) Tuj1 immunostaining and corresponding binarized images of axons of DRG neurons after 48 h of 30 nM or 600 nM paclitaxel or DMSO. Scale bar: 20  $\mu$ m. (B) Normalized area of axons after 48 h of 30 nM or 600 nM paclitaxel or DMSO applied to axons. Data represent mean  $\pm$  SEM; individual data points are shown. N represents number of images, with 10–20 images of each sample from one or two samples per experiment and three independent experiments. \*\*\*\*,  $P < 0.0001$  by one-way ANOVA with Tukey's multiple comparisons test. (C) Representative images of GCaMP6s (green) and mRuby3 (red) of axons of DRG neurons expressing tGFP shRNA (Ctl) or Sarm1 shRNA after 48 h of DMSO (Veh) or 600 nM paclitaxel (Pac) treatment. White arrowheads indicate axon with increased calcium at 36 h and degenerated at 48 h (also see Fig. 2 A). Scale bar: 20  $\mu$ m.

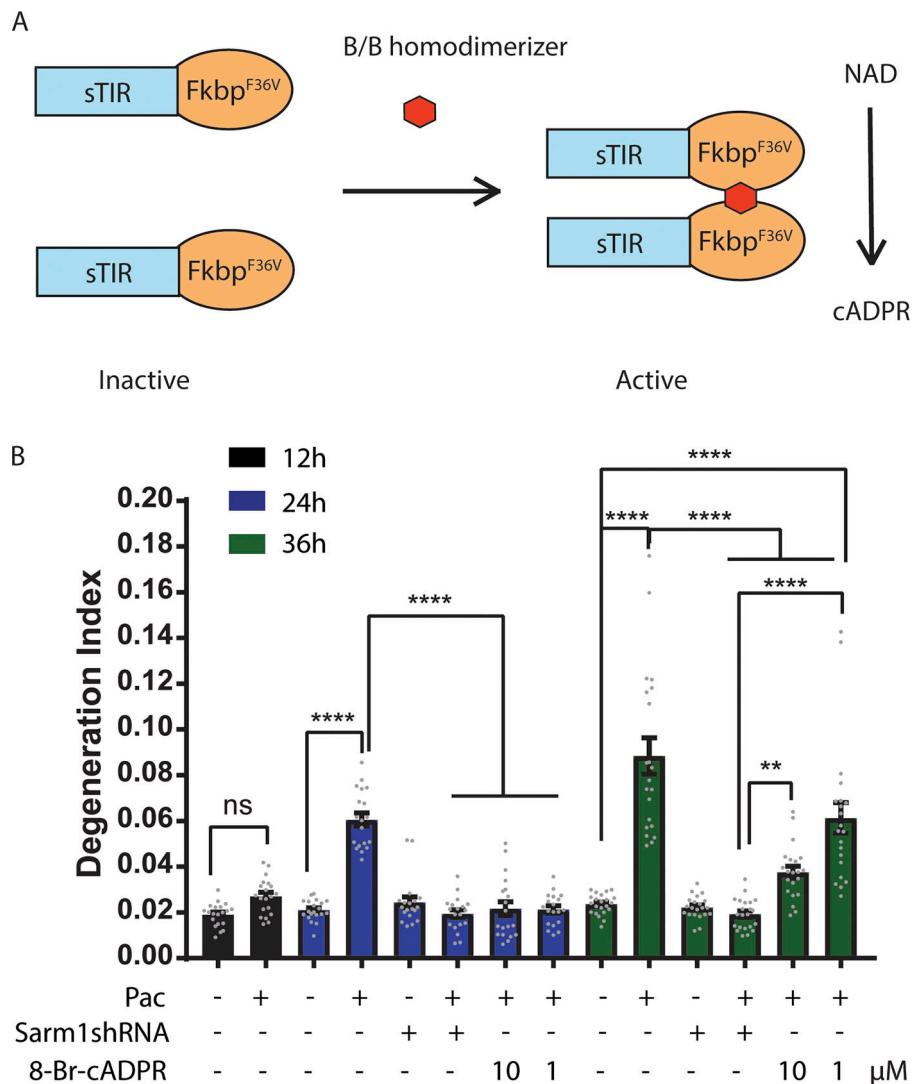


Figure S3. **Schematic illustration of chemical-induced sTIR dimerization and Sarm1 depletion provided stronger neuroprotection against paclitaxel than 8-Br-cADPR in vitro.** (A) Schematic illustration: B/B homodimerizer binds to Fkbp-F36V and triggers FkbpF36V-sTIR dimerization followed by NADase activation. (B) Degeneration index of DRG axons with or without Sarm1 shRNA expression after 12, 24, and 36 h of DMSO (Veh) or 30 nM paclitaxel (Pac) with pretreatment of indicated concentrations of 8-Br-ADPR. \*\*,  $P < 0.01$ ; \*\*\*\*,  $P < 0.0001$  by one-way ANOVA with Tukey's multiple comparisons test. Data represent mean  $\pm$  SEM; individual data points are shown. N represents number of images. Data pooled from three independent experiments.



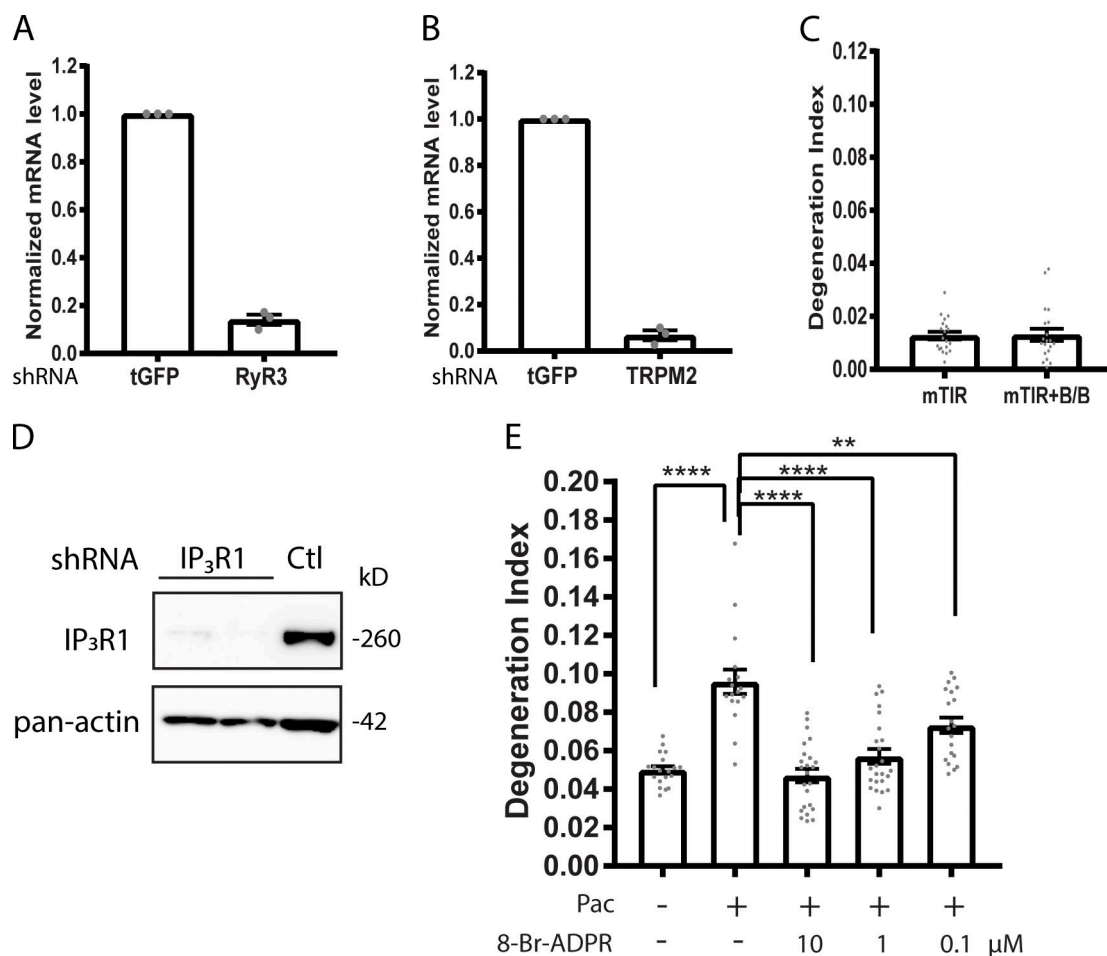
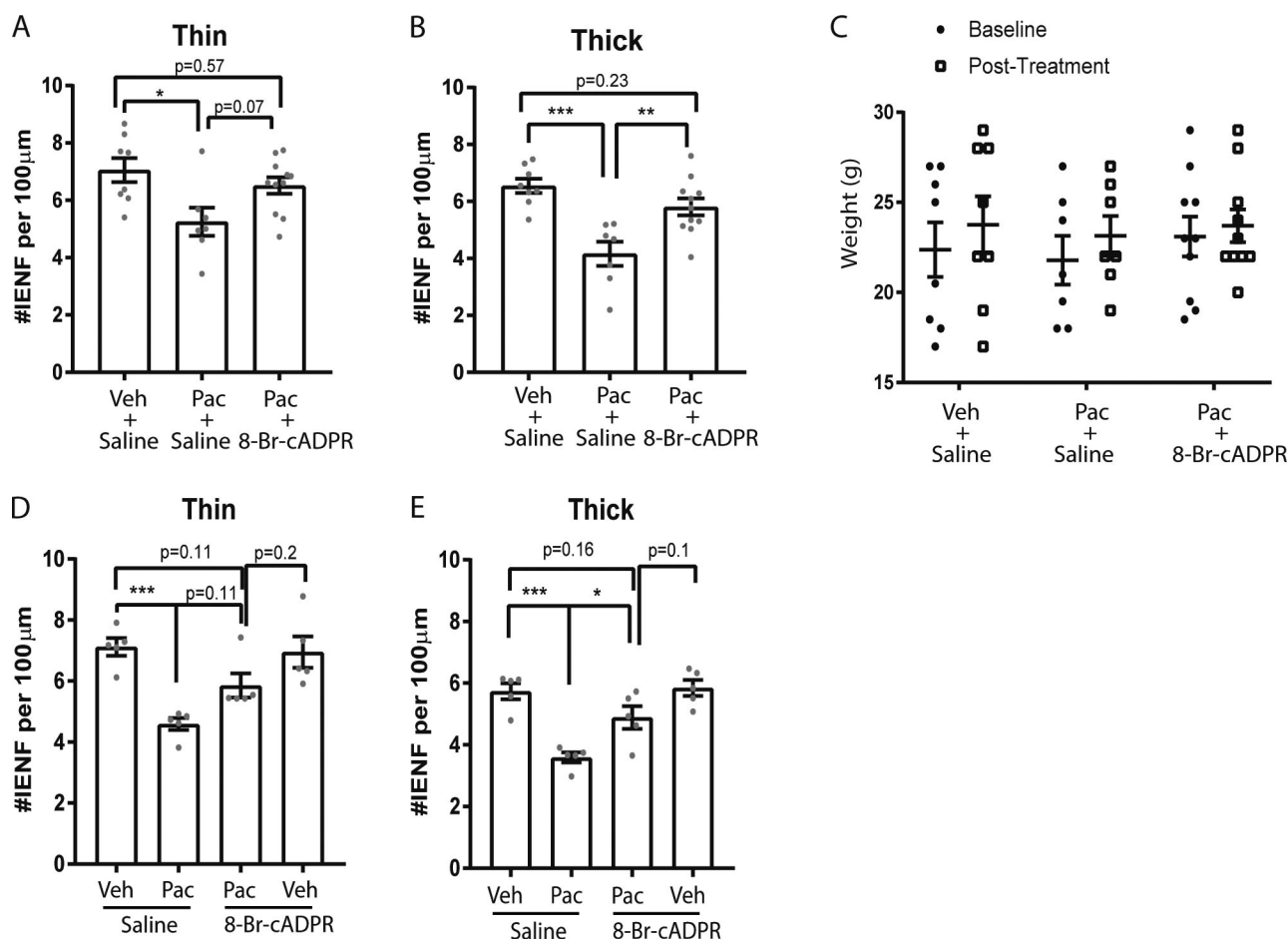


Figure S4. **Verification of knockdown by shRNAs targeted to RyR3, IP<sub>3</sub>R1, and TRPM2; mTIR dimerization does not cause axon degeneration; and 8-Br-ADPR protects against paclitaxel-induced axon degeneration in vitro.** (A and B) Normalized mRNA levels of DRG neurons showing knockdown efficiency of RyR3 shRNA (A) and TRPM2 shRNA (B). Data represent mean  $\pm$  SEM; individual data points are shown. N represents three independent experiments. (C) Degeneration index of DRG axons transduced with lentivirus expressing FkbpF36V-mTIR with or without 50 nM B/B homodimerizer treatment for 3 h. Data represent mean  $\pm$  SEM. N represents number of images. Individual data points are shown. Data pooled from three independent experiments. (D) Western blot probed against IP<sub>3</sub>R1 and pan-actin showing knockdown efficiency of IP<sub>3</sub>R1 shRNA in DRG neurons. (E) Degeneration index of DRG axons after 24 h of DMSO (Veh) or 30 nM paclitaxel (Pac) with indicated concentrations of 8-Br-ADPR. \*\*,  $P < 0.01$ ; \*\*\*\*,  $P < 0.0001$  by one-way ANOVA with Tukey's multiple comparison test. Data represent mean  $\pm$  SEM; individual data points are shown. N represents number of images. Data pooled from three independent experiments. Ctl, control.



**Figure S5. 8-Br-cADPR protects against paclitaxel-induced peripheral neuropathy in vivo without causing weight change of animals. (A and B)** Quantification of Tuj1-positive sensory fibers (green) entering the epidermis per 100- $\mu$ m epidermal length in nondermal papillae-containing thin (A) and dermal papillae-containing thick (B) skin isolated from normal mice treated with indicated drug combination. Data represent mean  $\pm$  SEM. N represents number of animals. Individual data point shown represents the mean of 6–10 images taken from individual animal (also see Fig. 6, D and E). **(C)** Body weights of animals before (Baseline) and after treatment (Post-treatment). Data represent mean  $\pm$  SEM; individual data points are shown. N represents number of animals. **(D and E)** Quantification of Tuj1-positive sensory fibers (green) entering the epidermis per 100- $\mu$ m epidermal length in nondermal papillae-containing thin (D) and dermal papillae-containing thick (E) skin isolated from E0771 cancer mice treated with indicated drug combination. Data represent mean  $\pm$  SEM. N represents number of animals. Individual data point shown represents the mean of 8–16 images taken from individual animal (also see Fig. 6, D and E). \*,  $P < 0.05$ ; \*\*,  $P < 0.01$ ; \*\*\*,  $P < 0.001$ . Pac, paclitaxel; Veh, vehicle.

Provided online are five tables. Table S1 presents statistical analysis of NAD level shown in Fig. 1 D. Table S2 presents statistical analysis of NADP level shown in Fig. 1 E. Table S3 presents statistical analysis of cADPR level shown in Fig. 1 F. Table S4 summarizes MRM transitions and retention time windows. Table S5 presents key resources.